

1 **Frictional and Hydraulic Properties of Plate Interfaces Constrained by**
2 **a Tidal Response Model Considering Dilatancy/Compaction**

3 **Ryunosuke Sakamoto¹ and Yoshiyuki Tanaka²**

4 ¹Department of Earth and Space Science, Osaka University, Osaka, Japan

5 ²Department of Earth and Planetary Science, University of Tokyo, Tokyo, Japan

6 Corresponding author: Ryunosuke Sakamoto (sakamoto@neq.ess.sci.osaka-u.ac.jp)

7 **Key points:**

- 8 • The spring-slider model with dilatancy/compaction reproduces the observed tidal
9 response of tremors during episodic tremor and slip (ETS).
- 10 • The critical slip distance, diffusivity and effective stress are constrained by a comparison
11 between the model and the observation.
- 12 • The pore fluid pressure change due to dilatancy/compaction is dominant at the early stage
13 of the ETS, while it is negligible at the later stage.

14

15 **Abstract**

16 Tidal triggering of tectonic tremors has been observed at plate boundaries around the circum-Pacific region. It has
17 been reported that the response of tremors to tidal stress during episodic tremor and slow slip (ETS) changes
18 between the early and later stages of ETS. Several physical models have been constructed, with which observations
19 for the tidal response during ETS have been partly reproduced. However, no model has been proposed that
20 reproduces all the observations. In this study, a model adopted in previous studies is extended to include the effects
21 of dilatancy/compaction that occur in the fault creep region. The analytical approximate solution derived in this
22 study and numerical computational results reveal how the tidal response depends on the physical properties of the
23 fault. Furthermore, the model reproduces all the above observations simultaneously for a specific range of fault
24 parameters. Of particular importance is that the occurrence of dilatancy/compaction is essential to reproduce the
25 tidal response at the early stage of the ETS. The value of the critical distance d_c is constrained to be approximately
26 1~10 cm. This agrees with the values that have been widely used in seismic cycle numerical simulations rather than
27 those obtained in laboratory experiments. The fluid pressure diffusivity is constrained to be at least 10^{-5} m²/s or
28 less, and the effective normal stress is constrained to $10^{5\sim6}$ Pa. In conclusion, this study shows that reproducing the
29 tidal response of tectonic tremors during the ETS is useful for estimating fault physical properties, including
30 hydraulic properties.

31 **Plain Language Summary**

32 Slow earthquakes, which are slower fault slips than ordinary earthquakes, have been observed at many plate
33 boundaries around the Pacific Rim. To understand how slow earthquakes occur, we need to know the exact physical
34 fault properties that cause slow earthquakes. Previous studies have reported that the rate of occurrence of tectonic
35 tremors, which are slow earthquakes, varies periodically in response to subsurface stress changes induced by tides.
36 However, the detailed mechanism of the periodic behavior is still unclear. In this paper, we develop a theoretical
37 model to explain this periodic behavior. A comparison between the observations in the Nankai Trough and Cascadia
38 with our model shows that the pore fluid pressure in the vicinity of the fault changes significantly when tremors
39 respond relatively weakly to tides. Furthermore, for the model to explain the observed tidal response of tremors, we
40 find that the scale of the surface roughness of the fault should be much larger than those obtained by laboratory
41 experiments and that the fault should have a low permeability.

42 **1 Introduction**

43 Recent geodetic and seismological observations have revealed that slow earthquakes occur in the transition zone,
44 which is located at the deeper extension of the locked megathrust zone in a subduction zone. Slow earthquakes have
45 various timescales, which are classified into low-frequency earthquakes (LFEs) with a major frequency of 2 – 8 Hz
46 (Obara, 2002), tectonic tremors, which are aggregations of LFEs (Shelly et al., 2007a), very low-frequency
47 earthquakes (VLFs) with a major frequency of 20 – 200 Hz (Ito et al., 2007), and slow slip events (SSEs), which
48 do not radiate seismic waves and continue to slip for more than a few days (Dragert et al., 2001; Hirose et al., 1999).
49 The focal mechanism of these slow earthquakes indicates that they accommodate shear slip on the plate interface
50 (e.g., Ide et al., 2007; Shelly et al., 2006). This focal mechanism coincides with that of ordinary earthquakes, which
51 are caused by fast slip. It is well known that the fast slip behavior of an ordinary earthquake reflects the physical
52 properties of the fault, which consist of friction, effective normal stress and dilatancy/compaction (e.g., Proctor et
53 al., 2020; Scholz, 2019; Segall and Rice, 1995). The coincidence of the focal mechanism with those of slow
54 earthquakes means that the slip behaviors of slow earthquakes should also reflect such fault physical properties.
55 Therefore, it is important to clarify the physical fault properties in the transition zone to reveal the mechanism of
56 slow earthquakes on various timescales.

57 In numerical simulation studies, several models have been proposed to reproduce slow earthquakes. These models
58 usually adopt the rate- and state-dependent friction law (RSF) (e.g., Dieterich, 1979; Marone, 1998) as the frictional
59 law on the plate interface. Examples of such models are those assuming near-neutral stability (e.g., Liu and Rice,
60 2005; Matsuzawa et al., 2010), dilatant strengthening of the shear zone (e.g., Liu, 2013; Segall et al., 2010),
61 transition from velocity weakening (VW) at a low slip rate to velocity strengthening (VS) at a high slip rate (e.g., Im
62 et al., 2020; Peng and Rubin, 2018; Shibazaki and Iio, 2003), spatial heterogeneity of frictional properties and
63 effective normal stress (Luo and Ampuero, 2018), and sudden negative Coulomb stress change in the VS region due
64 to fault valve action (Perfettini and Ampuero, 2008). Comparisons between such models and observed slow slip
65 behaviors have allowed us to estimate the physical fault properties in the transition zone, which cannot be observed
66 directly (e.g., Beeler et al., 2018; Luo and Liu, 2019; Nakata et al., 2012; Shibazaki et al., 2012).

67 In this study, we focus on tectonic tremors because they occur more frequently than other slow earthquakes, and it is
68 easier to obtain more data to investigate the physical properties of faults. Tremors are classified into episodic
69 families that accompany a SSE and continuous families that consist of tremors that occur almost daily (Thomas et

70 al., 2018). The former is called episodic tremor and slip (ETS) (Obara et al., 2004; Rogers and Dragert, 2003). An
71 important observation is that, for an ETS, there is a correlation between the slip rate of the SSE and the tremor
72 occurrence rate (e.g., Bartlow et al., 2011; Hirose and Obara, 2010; Thomas et al., 2018; Villafuerte et al., 2017),
73 even though the cumulative moment magnitude M_w of tremors is orders of magnitude smaller than that of SSEs
74 (Kao et al., 2010). This correlation has been modeled by assuming that a tremor source is driven to failure by the
75 stress loading due to aseismic slip that occurs in the region surrounding the tremor source (Shelly et al., 2007a).
76 Based on this model, Shelly et al. (2011) interpreted the delayed dynamic triggering of tremors as a result of
77 transient creep induced by the passage of seismic waves. Similarly, Tan and Marsan (2020) interpreted that the
78 spatial anisotropy of the SSE during an ETS causes anisotropy in the power law describing a spatial decay of
79 tremors.

80 Another important observational fact revealed by global observations of tremors is that tremors are sensitive to
81 tidal stress (e.g., Chen et al., 2018; Hoston, 2015; Ide and Tanaka, 2014; Ide et al., 2015; Nakata, 2008; Royer et al.,
82 2015; Rubinstein et al., 2008; Shelly et al., 2007b; Thomas et al., 2009, 2012; Van Der Elst et al., 2016; Yabe et al.,
83 2015).

84 In general, stress changes on faults due to semidiurnal and diurnal tides are a few kPa or smaller. These stress
85 changes are much smaller than the stress drop of ordinary earthquakes. Observational studies have reported that, in
86 some cases, a weak correlation can be seen between earthquakes and tidal stresses (e.g., Cochran et al., 2004;
87 Métivier et al., 2009; Tanaka 2010, 2012). The tidal response of earthquakes has also been studied by laboratory
88 experiments using a stress perturbation to rock or granular materials (e.g., Bartlow et al., 2012; Beeler and Lockner
89 2003; Chanard et al., 2019; Lockner and Beeler, 1999; Noël and Passelègue et al., 2019; Noël and Pimienta et al.,
90 2019; Savage and Marone, 2007). For example, the results of Chanard et al. (2019) and Noël and Pimienta et al.
91 (2019) are consistent with the observation results of Tanaka (2010, 2012) regarding the tidal response that appears
92 before a large earthquake. Other studies have reported that no correlation is seen between earthquakes and tidal
93 stresses (e.g., Heaton 1982; Vidale et al., 1998; Wein and Shearer 2004).

94 The tidal response of tremors is clearer because the pore fluid pressure on the plate interfaces is much higher in the
95 transition zone than in the seismogenic zone, and hence, the effective normal stress is extremely low (Audet et al.,
96 2009; Shelly et al., 2006).

97 The tidal response of tremors can be characterized by a tidal sensitivity and a phase difference. The tidal sensitivity,
 98 α , characterizes the magnitude of tidal modulation of the tremor rate (i.e., the number of observed tremor events per
 99 unit time); the relationship between the tremor rate and the tidal Coulomb stress change is described by

$$100 \quad R = R_0 e^{\alpha \Delta S(t)}, \quad (1)$$

101 where R denotes the tremor rate, $\Delta S(t)$ is the tidal Coulomb stress, and R_0 is the reference tremor rate when
 102 $\Delta S(t) = 0$. In equation (1), the order of the tidal sensitivity is $0.01 \sim 1 \text{ kPa}^{-1}$ (e.g., Houston, 2015; Ide et al., 2015;
 103 Royer et al., 2015; Thomas et al., 2012; Yabe et al., 2015). The phase difference, defined as δ , represents the phase
 104 shift between the tremor rate peak (i.e., the phase at which R is maximum) and the tidal stress peak (i.e., the phase at
 105 which $\Delta S(t)$ is maximized). δ is positive when the tremor rate reaches its maximum before the tidal stress reaches
 106 its maximum. For example, when the peak of R precedes the peak of $\Delta S(t)$ in the semidiurnal tide (approximately 12
 107 hour cycle) by 3 hours, $\delta \sim \pi/2$. Previous studies have reported that α and δ change at the early and later stages of
 108 the ETS (Houston, 2015; Royer et al., 2015; Yabe et al., 2015). At the early stage of an ETS, $\alpha \lesssim 0.1 \text{ kPa}^{-1}$
 109 (meaning that tidal modulation of the tremor rate is smaller) and $\delta \sim \pi/2$. At the later stage of the ETS, $\alpha \sim 0.7 \text{ kPa}^{-1}$
 110 (meaning that the tidal modulation of the tremor rate is larger) and $\delta \sim 0$. In addition, the number of tremors
 111 occurring at the later stage of ETS is approximately 1/10 or less than at the early stage of ETS (Houston, 2015;
 112 Royer et al., 2015).

113 Constructing a model that reproduces such observed tidal responses of tremors is an effective method to infer the
 114 physical properties of faults because tidal stress change, which serves as an “input” to a fault slip model to
 115 reproduce the tidal response, is much easier to estimate. Previous studies have proposed several models to interpret
 116 the observed tidal response of tremors (Ader et al., 2012; Beeler et al., 2013; Beeler et al., 2018; Hawthorne and
 117 Rubin, 2013; Houston, 2015). These models are classified into deterministic models that adopt the physical model
 118 proposed by Shelly et al. (2007a) and a stochastic model that adopts the Weibull distribution as the failure strength
 119 of tremor sources. Furthermore, deterministic models are classified into two models: one considers the change in the
 120 pore fluid pressure at the plate interface, and the other does not (Table 1).

121 Specifically, under the assumption that the tremor rate is proportional to fault creep velocity, Ader et al. (2012),
 122 Beeler et al. (2013) and Hawthorne and Rubin (2013) investigated the tidally modulated tremor rate. Ader et al.
 123 (2012) adopted the RSF for the VS to describe the tidal modulation of the fault creep velocity. They showed that the
 124 tidal sensitivity and the phase difference (the phase difference between the fault creep velocity peak and the tidal

125 stress peak) depend on the tidal period, fault creep velocity and frictional properties. Based on this result, they
 126 provided a framework to explain the tidal sensitivity and the phase difference in terms of tidal period, fault creep
 127 velocity and frictional properties. Beeler et al. (2013) compared dislocation creep, dislocation glide and the RSF for
 128 the VS region to explain the exponential relationship of equation (1) and concluded that the exponential behavior
 129 was derived from the RSF for the VS region. Based on a model that follows the RSF assuming a transition from the
 130 VW at a lower slip velocity to the VS at a higher slip velocity, Hawthorne and Rubin (2013) showed that the tidal
 131 modulation of the fault creep velocity increases as the fault creep average velocity decreases. Based on a
 132 probabilistic model, Houston (2015) interpreted that the tidal response of tremors is different between the early stage
 133 and later stages of ETS due to a gradual decrease in the fault strength for the tremor sources. Beeler et al. (2018)
 134 reproduced the observed tidal response of tremors of the continuous families based on a model assuming the RSF of
 135 the VW and estimated fault physical properties of the transition zone, such as the fluid pressure diffusivity and
 136 dilatancy coefficient.

137

138 Table 1. A summary of previous models and our model

Paper that proposed the model	Model type	Introduction of fluid pressure change by dilatancy/compaction	Reproduction of tidal response of tremor at the early stage of ETS	Reproduction of tidal response of tremor at the later stage of ETS
Ader et al. (2012)	Deterministic	No	Tidal period $> 10^8$ s	Yes
Beeler et al. (2013)	Deterministic	No	Cannot reproduce phase difference	Yes
Hawthorne and Rubin (2013)	Deterministic	No	Cannot reproduce phase difference	Yes
Houston (2015)	Probabilistic	—	Yes ^a	Yes ^a
Beeler et al. (2018)	Deterministic	Yes	— ^b	— ^b
This study	Deterministic	Yes	Yes	Yes

139 ^a The model assumption may not be valid. ^b The model is not applicable to the tidal modulation of tremors during

140 ETS.

141
142 Most of the above models only partially explain the observations of the tidal response of tremors during ETS with
143 several advantages (Table 1). Ader et al. (2012) investigated the slip behavior of a one-degree-of-freedom spring-
144 slider system under a harmonic stress perturbation with different periods. Their model could reproduce the tidal
145 response of tremors at the later stage of the ETS when considering diurnal and semidiurnal tidal periods ($\sim 10^5$ s).
146 However, the model could not reproduce the phase difference of $\delta \sim \pi/2$ observed at the early stage of ETS unless
147 adopting much longer tidal periods (e.g., 18.6 years tide) ($> 10^8$ s). Beeler et al. (2013) and Hawthorne and Rubin
148 (2013) modeled the tidal modulation of fault creep velocity using a purely rate-dependent friction law and a
149 frictional law assuming a transition from the VW to VS region, respectively. Their results show that the fault creep
150 velocity increases as the tidal stress increases. This suggests that these models could explain the tidal response of
151 tremors at the later stage of the ETS but not the phase difference observed at the early stage of the ETS ($\delta \sim \pi/2$).
152 The model of Houston (2015) assumes that breakage of mineral precipitates due to slip accumulation during the ETS
153 might weaken the fault strength. This model may contradict the idea of dilatant strengthening, which assumes that
154 fault strength increases with increasing pore space due to breakage of precipitating minerals (Audet and Bürgmann,
155 2014). Beeler et al. (2018) modeled the correlation between LFE clusters and tidal stress for continuous families.
156 Their model focused only on the onset of the clusters. Therefore, their model cannot be applied to the tidal
157 modulation of tremors that lasts for 1~2 weeks during ETS. Therefore, the models proposed thus far cannot fully
158 explain the aspects of the observed tidal responses of tremors.

159 Here, we propose a new model in which dilatancy/compaction occurs in the VS region to explain the observed tidal
160 response of tremors during the ETS. We find that the pore fluid pressure changes due to dilatancy/compaction
161 caused by tidal stress change in the transition zone, where the effective normal stress is low, have a significant
162 influence on the sliding behavior in the VS zone. We present governing equations for this problem in section 2. In
163 the next section, we derive an approximate solution to quantitatively describe α and δ and clarify how the model
164 responds to tidal stress changes. We reveal the physical reason for the dependence of α and δ on the fault physical
165 properties. In section 4, we estimate fault physical properties based on a comparison between the observations and
166 our model results and discuss the validity of the estimated properties. In section 5, we summarize the results.

167 2 Methods

168 2.1 Modeling the rate of tremor occurrence

169 Similar to previous studies, we assume that tremors are generated by the rupture of small brittle patches on the fault
 170 plane due to the aseismic shear slip of a larger-scale surrounding fault (Ader et al., 2012; Beeler et al., 2013; Shelly
 171 et al., 2007a). This assumption means that the tremor source is very small and that the tremor rate, R , serves as a
 172 passive meter of the creep velocity of the surrounding fault, V :

$$173 \quad \frac{V}{V_r} = \frac{R}{R_r}, \quad (2)$$

174 where R_r and V_r denote the tremor rate and the creep velocity at a reference state, respectively. Based on this
 175 assumption, we can regard a change in the tremor rate as a change in the creep velocity. Equation (2) has been
 176 adopted in previous studies that modeled the tidal response of tremors and LFEs (e.g., Ader et al., 2012; Beeler et
 177 al., 2013).

178 2.2 Governing equations

179 2.2.1 Rate- and state-dependent friction law

180 We model the above fault creep, assuming a one-degree-of-freedom spring-slider system and employ the RSF as a
 181 friction law (Ader et al., 2012). According to the RSF, the friction coefficient μ can be written as:

$$182 \quad \mu = \mu_0 + a \log\left(\frac{V}{V_0}\right) + b \log\left(\frac{V_0 \theta}{d_c}\right), \quad (3)$$

183 where μ_0 denotes the friction coefficient at a reference slip velocity V_0 , V is the slip velocity, d_c is the critical slip
 184 distance, θ is the state variable, which is often interpreted as the average contact time for an asperity, and a and b
 185 are fault constitutive parameters (e.g., Scholz, 1998). To represent fault creep, the constitutive parameters must
 186 satisfy $a > b$. This regime is called VS. In equation (3), the second term on the right-hand side (RHS) represents the
 187 “direct effect”, which is caused by a change in the slip velocity, and the third term on the RHS represents the
 188 “evolution effect”, which is caused by the temporal change in the state variable. Fault slip behavior evolves to a new
 189 steady state when a sudden slip velocity change occurs and the fault slips over a distance of d_c (Dieterich, 1979).
 190 This process can be expressed in several ways. In this study, we adopt the slip law proposed by Ruina (1983):

$$191 \quad \frac{d\theta}{dt} = -\frac{V\theta}{d_c} \log\left(\frac{V\theta}{d_c}\right). \quad (4)$$

192 2.2.2 Dilatancy/Compaction

193 Dilatancy/compaction is a mechanism that relates fault gouge deformation to the behavior of the pore fluid. A
 194 shear zone exists at and near the plate interface where shear slip is localized and fault gouge is present (e.g., Rice,
 195 2006). We assume that the porosity change in the shear zone is caused by dilatancy/compaction (e.g., Segall et al.,
 196 2010; Suzuki and Yamashita, 2009). The associated behavior of pore fluids can be modeled as in the following two
 197 cases. The first is an undrained model, which assumes that the pore fluid pressure changes only within the shear
 198 zone (Figure S1a in the supporting information), and the second is a drained model, which assumes a “homogeneous
 199 diffusion” of the pore fluid into a region adjacent to the shear zone (Segall et al., 2010) (Figure S1b in the supporting
 200 information). Since our model is a one-degree-of-freedom system, the pore fluid pressure is uniform in the direction
 201 of the slip plane, and the pore fluid pressure diffuses in the direction perpendicular to the slip plane. The pore fluid
 202 pressure in the shear zone is spatially uniform in both the drained and undrained models. Let a tidal period be T
 203 (e.g., 12.4 hours) and the characteristic timescale at which the pore fluid pressure diffuses through the shear zone be
 204 t_w . The undrained model is valid when $T \ll t_w$ (Beeler et al., 2018), and the drained model is valid when $T \gg t_w$
 205 (Segall et al., 2010). As described later (section 4.2), the undrained model can explain the tidal response at the early
 206 and later stages of the ETS, while the drained model cannot explain the tidal response at the early stage of the ETS.
 207 We focused on the results for the undrained model in the main text, which can reproduce more observations than the
 208 drained model. The derivation of the governing equations and results for the drained model are shown in the
 209 supporting information (Texts S1-S4, Figures S3, S4 and S6).

210 Mathematically, in the undrained model, the pore fluid pressure change in the shear zone can be described as

$$211 \quad \frac{dp}{dt} = -M \frac{d\phi}{dt}, \quad (5)$$

212 which is derived from the conservation of pore fluid mass (Segall et al., 1995), where dp/dt denotes a temporal
 213 change in the pore fluid pressure, M is the bulk modulus of the fluid and the pore space, and $d\phi/dt$ denotes a
 214 change in the porosity due to dilatancy/compaction. As described previously, for the friction coefficient (equation
 215 (3)), the porosity, which varies with dilatancy/compaction, also evolves from one steady state to another as the slip
 216 velocity changes. The evolution law for the porosity can be empirically described as

217
$$\frac{d\phi}{dt} = -\frac{\epsilon}{\theta} \frac{d\theta}{dt}, \quad (6)$$

218 using the state variable θ , where ϵ is a dilatancy coefficient (Segall and Rice, 1995). From equations (5) and (6), we
219 obtain

220
$$\frac{dp}{dt} = \epsilon M \frac{1}{\theta} \frac{d\theta}{dt}. \quad (7)$$

221

222 2.2.3 A quasi-static equation of motion

223 The quasi-static equation of motion for the one-degree-of-freedom spring-slider model under tidal stress can be
224 written as

225
$$\Delta\tau(t) + k\Delta u = \mu\sigma_{eff}(t), \quad (8)$$

226 where $\Delta\tau(t)$ denotes the shear stress acting on the fault plane due to tides, $\sigma_{eff}(t)$ is the effective normal stress, Δu
227 is the relative displacement of the block to the spring pulling distance, k is the spring stiffness and μ is the friction
228 coefficient (Ader et al., 2012; Perfettini and Schmittbuhl, 2001). In our model, the effective normal stress is written
229 as $\sigma_{eff}(t) = \sigma_{eff}^0 + \Delta\sigma(t) - \Delta p(t) - \Delta p'(t)$, where σ_{eff}^0 denotes a reference effective normal stress, $\Delta\sigma(t)$ is the
230 normal stress acting on the fault plane due to tides, $\Delta p(t)$ is the pore fluid pressure change due to
231 dilatancy/compaction in the shear zone, and $\Delta p'(t)$ is the pore fluid pressure change due to the tidal normal stress
232 change. When the tidal normal stress increases, $\Delta p'(t)$ also increases in proportion to the Skempton coefficient, B
233 (i.e., $\Delta p'(t) = B\Delta\sigma(t)$) (e.g., Beeler et al., 2018; Scholz et al., 2019). Using this relationship, the effective normal
234 stress can be rewritten as

235
$$\sigma_{eff}(t) = \sigma_{eff}^0 + (1 - B)\Delta\sigma(t) - \Delta p(t). \quad (9)$$

236 The observations show that there is almost no correlation between the tidal normal stress change and the tremor
237 rate (Houston, 2015; Thomas et al., 2012), which indicates that the fault strength is almost unchanged due to the
238 tidal normal stress change. This suggests that B is nearly equal to 1 (equation (9)). Therefore, we adopt $B = 0.9$ in
239 our model. For simplicity, we assume that the tidal stresses $\Delta\sigma(t)$ and $\Delta\tau(t)$ have a common period with the same
240 magnitude and phase (i.e., $\Delta\sigma(t) = \Delta\tau(t) = |\Delta\sigma(t)|e^{i\omega t}$).

241

242 2.3 Nondimensionalization of governing equations

243 Equations (3), (4), (7) and (8) constitute the governing equations for our model. For nondimensionalization of these
 244 equations, we selected a tidal period T , a reference effective normal stress σ_{eff}^0 , and a critical slip distance d_c as
 245 characteristic physical quantities (Table 2). Representing the dimensionless variables with a tilde, the result is
 246 written as:

$$\begin{aligned}
 247 \quad \mu &= \mu_0 + a \log\left(\frac{\tilde{V}}{\tilde{V}_0}\right) + b \log\left(\frac{\tilde{\theta}}{\tilde{\theta}_0}\right) \\
 248 \quad \Delta \tilde{\tau} + \tilde{K} \Delta \tilde{u} &= \mu \tilde{\sigma}_{eff} \\
 249 \quad \frac{d\tilde{\theta}}{d\tilde{t}} &= -\tilde{\theta} \tilde{V} \log(\tilde{\theta} \tilde{V}) \\
 250 \quad \frac{d\tilde{p}}{d\tilde{t}} &= \frac{U}{\tilde{\theta}} \frac{d\tilde{\theta}}{d\tilde{t}}, \tag{10}
 \end{aligned}$$

251 where $\theta_0 = d_c/V_0$ denotes the state variable at a reference slip velocity V_0 , $\tilde{K} = d_c k / \sigma_{eff}^0$ is the nondimensional
 252 spring constant, and $U = M\epsilon / \sigma_{eff}^0$ is the dilatancy parameter. Substituting the last equation in equation (10) into the
 253 nondimensionalized version of equation (9), we find that the larger U is, the more dominant the effect of $\Delta p(t)$ on
 254 the effective normal stress is. In other words, the parameter U represents the relative importance of the
 255 dilatancy/compaction to the effective normal stress change. Previous experiments and observations suggest that
 256 $\sigma_{eff}^0 \sim 10^{5\sim 6}$ Pa (Nakata et al., 2008; Shelly et al., 2006; Yabe et al., 2015), $\epsilon \sim 10^{-4\sim -5}$ (Samuelson et al., 2009),
 257 and $M \sim 10^{10}$ Pa (Segall et al., 1995). This yields a possible range of U from 10^0 to 10^{-2} .

258 The time evolution of each physical quantity is numerically calculated using the fourth-order Runge–Kutta method.

259

260 Table 2. Parameters of fault physical properties

Parameter	Value
Reference velocity V_0	10^{-9} m/s
Spring pulling velocity V_{pl}	10^{-8} m/s
Reference frictional coefficient μ_0	0.7
Reference effective normal stress σ_{eff}^0	500 kPa

Skempton coefficient B	0.9
Spring stiffness k	10^4 Pa/m
Magnitude of tidal shear stress $ \Delta\tau(t) $	1 kPa
Magnitude of tidal normal stress $ \Delta\sigma(t) $	1 kPa
Tidal period T	12.4 h
Frictional parameter a	0.003
Frictional parameter b	0.002
Dilatancy parameter U	10^{-2-0}

261

262

2.4 Definition of the tidal sensitivity (α) and the phase difference (δ)

263 In previous studies, α has been estimated using equation (1), and δ has been inferred using the phase difference
 264 between the tidal Coulomb stress peak and the tremor rate peak (Houston, 2015; Royer et al., 2015; Yabe et al.,
 265 2015); we define α and δ in the same way. In the following, we refer to these two parameters as the “tidal
 266 response”.

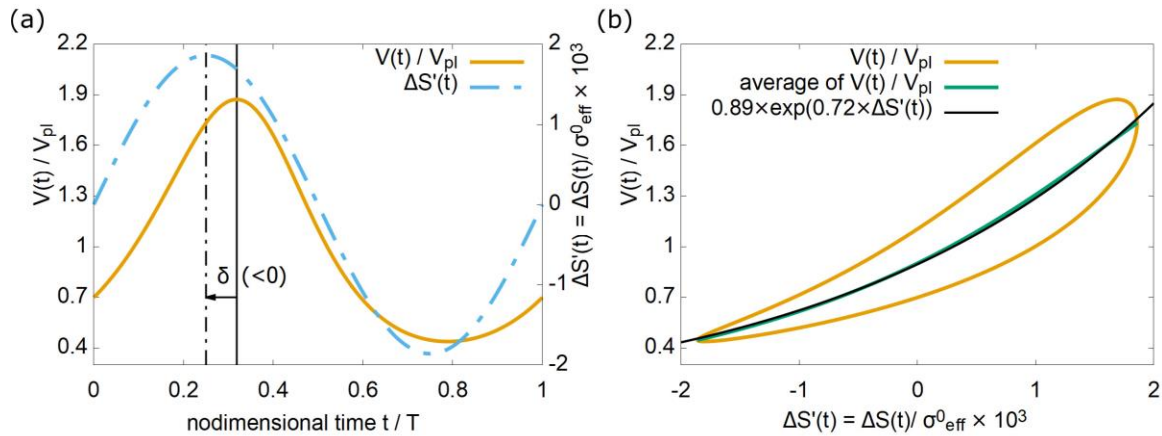
267 To illustrate the definition of these two quantities and how to determine them, Figure 1 shows a result obtained by
 268 numerically solving the governing equations for the case of $U = 0$ and $d_c = 100$ μm . The solid yellow line in
 269 Figure 1a is the time evolution of $V(t)/V_{pl}$ during one tidal cycle. The solid yellow line in Figure 1b shows
 270 $V(t)/V_{pl}$ in Figure 1a against the tidal Coulomb stress change $\Delta S(t)$, and the solid green line shows the average of
 271 the upper and the lower values of $V(t)/V_{pl}$ at each $\Delta S(t)$ on the horizontal axis, where

$$272 \quad \Delta S(t) = \Delta\tau(t) - \mu_{pl}(1 - B)\Delta\sigma(t) \quad (11)$$

273 (e.g., Beeler et al., 2018; Scholz et al., 2019), and μ_{pl} is the steady-state friction coefficient at velocity V_{pl} . The
 274 reason why $\Delta S(t)$ is described by $\Delta\tau(t) - \mu_{pl}(1 - B)\Delta\sigma(t)$ instead of $\Delta\tau(t) - \mu_{pl}\Delta\sigma(t)$ is that, for a poroelastic
 275 medium, the effective normal stress change due to tides is described by $(1 - B)\Delta\sigma(t)$ from equation (9). α is
 276 obtained by fitting the following equation to the average of $V(t)/V_{pl}$ (solid green line in Figure 1b):

$$277 \quad \frac{V(t)}{V_{pl}} = ce^{\alpha\Delta S(t)}. \quad (12)$$

278 In the fitting, a constant $c (< 1)$ is simultaneously determined. If c is not estimated, the following problem arises.
 279 Since our model pulls the block through the spring with velocity V_{pl} , the block must slip with V_{pl} on a long-term
 280 average ($\int_0^T V(t) dt/T = V_{pl}$ with $T \gg 0$). Equation (12) shows $V(t) \propto e^{\Delta S(t)}$, indicating that the slip velocity
 281 increases nonlinearly with $\Delta S(t)$. If $V(t) = V_{pl}$ at $S(t) = 0$ (equivalently $c = 1$), it is unphysical
 282 because $\int_0^T V(t) dt/T > V_{pl}$. Therefore, $V(t) < V_{pl}$ at $S(t) = 0$ (equivalently $c < 1$) is needed. The parameter c
 283 adjusts the average velocity but has nothing to do with the estimation of fault physical properties in the following.
 284 Figure S2 shows the obtained value of c . The solid black line in Figure 1b shows the fitted result. δ is defined as the
 285 phase difference between the $\Delta S(t)$ peak and the $V(t)/V_{pl}$ peak (see δ of Figure 1a), where δ is positive when the
 286 $V(t)/V_{pl}$ peak precedes the $\Delta S(t)$ peak (i.e., δ in Figure 1a is negative).
 287



288
 289 Figure 1. The numerical solution of equation (10) for $U = 0$ and $d_c = 100 \mu\text{m}$. (a) Determination of the phase
 290 difference (δ). The horizontal axis denotes time normalized by the tidal cycle, and the value from 0 to 1 indicates
 291 one tidal cycle. The vertical axis represents the slip velocity normalized by the reference velocity, $V(t)/V_{pl}$. The
 292 solid yellow line shows $V(t)/V_{pl}$, and the dashed blue line shows the tidal Coulomb stress, $\Delta S(t) \times 10^3$, normalized
 293 by the reference effective normal stress, σ_{eff}^0 . The dashed black line represents the phase when $\Delta S(t)$ reaches the
 294 maximum, and the solid black line represents the $V(t)/V_{pl}$ peak. The phase difference δ is defined so that it is
 295 positive when the $V(t)/V_{pl}$ peak precedes the $\Delta S(t)$ peak. (b) Determination of the tidal sensitivity (α). The
 296 horizontal axis is $\Delta S'(t) = \Delta S(t)/\sigma_{eff}^0 \times 10^3$. The vertical axis represents the slip velocity normalized by the
 297 reference velocity, $V(t)/V_{pl}$. The solid yellow line shows $V(t)/V_{pl}$ in (a). The solid green line shows the average of

298 the upper and lower velocities at each value of $\Delta S'(t)$. c and α in equation (12) are determined by a least squares
 299 method by fitting equation (12) against the green solid line. The solid black line shows the fitted result ($\alpha =$
 300 $0.72, c = 0.89$).

301

302 2.5 An approximate solution for α and δ

303 To clarify how the tidal responses depend on the fault physical properties, we analytically derived an approximate
 304 solution for α and δ . The result is shown in section 3.1.

305 3 Result

306 3.1 Derivation and verification of the approximate solution

307 When the magnitude of the tidal Coulomb stress change $|\Delta S(t)|$ is small enough ($|\Delta S(t)| \ll (a - b)\sigma_{eff}^0$), we
 308 assume that the perturbation of each physical quantity caused by $|\Delta S(t)|e^{i\omega t}$ is proportional to $e^{i\omega t}$, where $\omega =$
 309 $2\pi/T$ is the angular velocity of the tide (Segall, 2010; Ader et al., 2012). In other words, the physical quantities can
 310 be written as $V(t) = V_{pl} + \Delta V e^{i\omega t}$, $\theta(t) = \theta_{pl} + \Delta\theta e^{i\omega t}$ and $p(t) = p_0 + \Delta p e^{i\omega t}$, where θ_{pl} denotes the steady-
 311 state variable at $V = V_{pl}$, p_0 is the reference value of pore fluid pressure, and ΔV , $\Delta\theta$ and Δp are the magnitudes of
 312 the perturbation. Substituting these forms into equations (3), (4), (7), and (8), and after some algebra, the
 313 perturbation of the nondimensionalized slip velocity, $\Delta\tilde{V}$, can be written as

$$314 \frac{\Delta\tilde{V}}{\tilde{V}_{pl}} = \frac{2\pi i}{\tilde{K}\tilde{V}_{pl} + 2\pi i A} |\Delta\tilde{S}(t)|, \quad (13)$$

315 where

$$316 A = a - \frac{1}{1 + i\frac{T_\theta}{T}} (b - \mu_{pl}U) \quad (14)$$

317 and

$$318 T_\theta = 2\pi \frac{d_c}{V_{pl}}. \quad (15)$$

319 Equation (15) represents a characteristic timescale on which the state variable evolves (Ader et al., 2012). From the
 320 relationship of $\Delta\tilde{V}e^{i\omega t} = \tilde{V}(t) - \tilde{V}_{pl}$, equations (13) and (14) can be rewritten as $\tilde{V}(t)/\tilde{V}_{pl} = 1 +$
 321 $2\pi i\Delta\tilde{S}(t)/(\tilde{K}\tilde{V}_{pl} + 2\pi iA)$. We assume that this equation is the Taylor expansion of the RHS of

$$322 \quad \frac{\tilde{V}(t)}{\tilde{V}_{pl}} = \exp\left(\frac{2\pi i}{\tilde{K}\tilde{V}_{pl} + 2\pi iA}\Delta\tilde{S}(t)\right) \quad (16)$$

323 to the first order. Then, comparing equation (16) with equation (1), we find that the tidal sensitivity (α) and the
 324 phase difference (δ) can be written as

$$325 \quad \alpha = \text{Re}\left(\frac{2\pi i}{(\tilde{K}\tilde{V}_{pl} + 2\pi iA)\sigma_{eff}^0}\right) \quad (17)$$

$$326 \quad \delta = \arg\left(\frac{2\pi i}{\tilde{K}\tilde{V}_{pl} + 2\pi iA}\right) \quad (18)$$

327 For $U = 0$, where dilatancy/compaction is neglected, Ader et al. (2012) presented a linearized approximation
 328 solution and a numerical solution. We confirmed that equations (13) and (18) are consistent with the
 329 nondimensionalized version of equation (3) of Ader et al. (2012), who examined tidal responses for different values
 330 of T . However, how the tidal response changes with different values of d_c was not studied in detail for the period of
 331 ~ 12 h, which is the dominant period of tides. Therefore, we examined how the tidal response changes with changes
 332 in d_c or T_θ (equation (15)) for this period, since a comparison between our model and observations of the tidal
 333 response enables us to infer d_c in the actual geophysical situation. Figures 2a and 2b show α and δ , respectively. In
 334 these figures, the solid green line and green dots represent the numerical solution of equation (10) and the
 335 approximate solution, respectively. The approximate solution and the numerical solution agree with each other
 336 within 15% for most cases. When $T_\theta/T \sim 10^{-1}$, the approximate solution is less accurate for both α and δ . This
 337 means that the accuracy of the approximate solution can deteriorate when the nonlinearity is stronger (i.e., α is
 338 larger).

339 For $U \neq 0$, the approximate solution agrees with the numerical solution within 10% for all cases (the deviation
 340 between the approximate and numerical solutions is the maximum when $T_\theta/T \sim 140$ and $U = 1$. In this case,
 341 $\delta \sim 1.134$ for the numerical solution and $\delta \sim 1.023$ for the approximate solution, resulting in a relative error of
 342 $\sim 9.7\%$). The good agreement is attributed to the fact that α is relatively small (at most ~ 0.7 kPa $^{-1}$); thus, the
 343 nonlinearity is weaker. This indicates that the approximate solution is valid regardless of the value of T_θ/T when
 344 $U \neq 0$.

345 3.2 Dependence of the tidal response on the fault physical properties

346 Based on the approximate solution and an analysis of the quasi-static equation of motion, we clarify how α and δ
 347 during an ETS depend on the fault physical properties. The specific range of physical properties that can explain the
 348 observations is discussed in section 4.

349 3.2.1 Factors governing the tidal response during the ETS

350 We assume that the VS region surrounding tremor patches slides at an average velocity of V_{pl} . In our
 351 spring-slider model, this situation is represented by setting the velocity of the pulling spring to V_{pl} . We can
 352 apply this model to fault creep during the ETS, which occurs over a shorter time span than secular plate subduction.
 353 Geodetic observations show that the fault creep velocity during an ETS is $\sim 10^{-6\sim-9}$ m/s (e.g., Meade and
 354 Loveless, 2009; Schwartz and Rokosky, 2007). Therefore, we set V_{pl} as 10^{-8} m/s in the following numerical
 355 simulation. In addition, the frictional parameters a and b are chosen so that $a - b$ is small because it has been
 356 suggested that $a - b$ decreases in the transition zone (e.g., Liu, 2013; Matsuzawa et al., 2010). The other parameters
 357 are similar to those used in previous studies (Ader et al., 2012; Hawthorne and Rubin, 2013). Table 2 shows the
 358 adopted parameters. For these parameters, we can confirm that $|\tilde{K}\tilde{V}_{pl}| \ll |2\pi iA|$. Then, the tidal response (equations
 359 (17) and (18)) can be approximated as

$$360 \alpha \sim \text{Re}\left\{(A\sigma_{eff}^0)^{-1}\right\} \quad (19)$$

$$361 \delta \sim \text{arg}\{A^{-1}\}. \quad (20)$$

362 Combining these equations with equation (14), we note that α and δ depend on T_θ/T and U . The former parameter
 363 T_θ/T prescribes the response of the state variable to the tide, which is uniquely determined once we determine V_{pl} ,
 364 d_c and T . T_θ/T is constant throughout the tidal cycle. $T_\theta/T \ll 1$ means that the state variable is close to the steady
 365 state value (d_c/V) throughout a tidal cycle, and $T_\theta/T \gg |b - \mu_{pl}U|/a$ means that the state variable is almost
 366 constant throughout a tidal cycle (see section 3.2.3 for more details). In the following, we focus on these two
 367 parameters, T_θ/T and U , to discuss the tidal response.

368 3.2.2 A balance of the stress changes

369 From Figures 2a and 2b, we see a large difference between the cases for $U = 0$ and $U \neq 0$. The reason for this
 370 large difference can be understood by using the following equation, which is derived from the quasi-static equation
 371 of motion (equation (8)) (for the derivation, see Appendix A):

$$372 \quad \Delta S(t) \sim \sigma_{eff}^0 \left(-\mu_{pl} U \ln \left(\frac{\theta}{\theta_{pl}} \right) + a \ln \left(\frac{V}{V_{pl}} \right) + b \ln \left(\frac{\theta}{\theta_{pl}} \right) \right). \quad (21)$$

373 In equation (21), the left-hand side (LHS) and RHS correspond to the tidal Coulomb stress and frictional strength,
 374 respectively. The first, second, and third terms on the RHS represent the dilatancy/compaction effect, the direct
 375 effect, and the evolution effect, respectively. When $U = 0$, the first term vanishes, and the tidal response (equations
 376 (19) and (20)) obtained in this study is consistent with the result discussed in Chapter 4.1 of Hawthorne and Rubin
 377 (2013). Therefore, we analyze the tidal response for $U \neq 0$ below.

378 3.2.3 Analysis of the tidal response for $U \neq 0$

379 Figures 2a and 2b show that the tidal response can be classified into three cases according to the value of T_θ/T
 380 because the value affects the degree to which the first term of $a\{1 - (b - \mu_{pl}U)/a(1 + iT_\theta/T)\}$ is dominant (see
 381 equation (14)). The condition for the first term on the RHS of equation (14) to be negligibly small is $|b -$
 382 $\mu_{pl}U|/a|1 + iT_\theta/T| \ll 1$. Using the parameter set shown in Table 2, we obtain $|b - \mu_{pl}U|/a \sim O(1)$, so $T_\theta/T \gg$
 383 $|b - \mu_{pl}U|/a$ is required for the above inequality to hold. Conversely, the condition for the first term on the RHS of
 384 equation (14) becoming dominant is when the value of $a(1 + iT_\theta/T)$ becomes $\sim a$. In other words, $T_\theta/T \ll 1$. The
 385 other case is the intermediate region between these two limits.

386 First, we consider the case where $T_\theta/T \gg |b - \mu_{pl}U|/a$. We find that for larger values of T_θ/T , α and δ converge
 387 to the same values regardless of the value of U ($T_\theta/T \sim 10^4$ in Figures 2a and 2b). When $T_\theta/T \gg |b - \mu_{pl}U|/a$, the
 388 first term on the RHS of equation (14) can be ignored ($A \sim a$). Therefore, substituting $A \sim a$ into equations (19) and
 389 (20), α and δ become $a\sigma_{eff}^0$ and 0, respectively, regardless of the value of U . Because the state variable evolves
 390 more slowly than the tidal Coulomb stress change, the state variable is almost constant ($\theta \sim \theta_{pl}$) throughout a tidal
 391 cycle. Then, the dilatancy/compaction and the evolution effect term of equation (21) are almost zero. Therefore,
 392 equation (21) can be approximated as $\Delta S(t) \sim a\sigma_{eff}^0 \log(V/V_{pl})$ or $V \sim V_{pl} e^{\Delta S(t)/a\sigma_{eff}^0}$. This means that $\alpha = 1/a\sigma_{eff}^0$.

393 Moreover, the form of this equation indicates that the slip velocity peak agrees with the tidal Coulomb stress peak in
 394 time, which means that $\delta = 0$.

395 Next, we consider the case where $T_\theta/T \ll 1$. In this case, α depends on U and takes a small value when U is large
 396 ($T_\theta/T \sim 10^{-2}$ in Figure 2a). However, δ converges to zero regardless of the value of U ($T_\theta/T \sim 10^{-2}$ in Figure 2b).
 397 When $T_\theta/T \ll 1$, we obtain $\alpha = 1/(a - b + \mu_0 U)\sigma_{eff}^0$ and $\delta = 0$ from equations (14), (19) and (20). Because the
 398 state variable evolves more rapidly than the tidal Coulomb stress change, the state variable is close to the steady
 399 state value ($\theta \sim d_c/V$) throughout a tidal cycle. This is derived by considering $d\theta/dt \sim 0$ in equation (4). Then,
 400 equation (21) can be approximated as $\Delta S(t) \sim (a - b + \mu_{pl} U)\sigma_{eff}^0 \log(V/V_{pl})$. As before, the form of this equation
 401 explains the above values of α and δ . Moreover, it is clear from the form of α that it decreases as U increases.

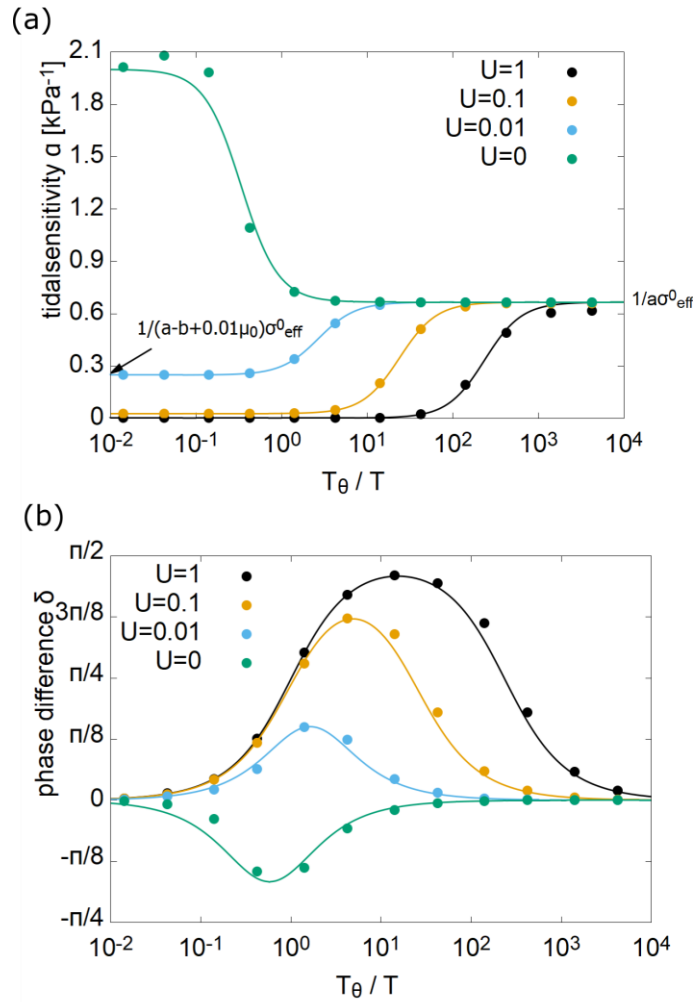
402 Finally, we consider the case of the intermediate region between the above two limit cases ($T_\theta/T \ll 1$ and $T_\theta/T \gg$
 403 $|b - \mu_{pl} U|/a$). Figure 2a shows that α varies smoothly and connects the limit values for $T_\theta/T \gg |b - \mu_{pl} U|/a$ and
 404 $T_\theta/T \ll 1$ ($T_\theta/T \sim 10^{0 \sim 1}$ in Figure 2a). Figure 2b shows that the maximum value of δ approaches $\pi/2$ as U
 405 increases ($T_\theta/T \sim 10^{0 \sim 1}$ in Figure 2b). To clarify why this occurs, we compared the time variation of the tidal
 406 Coulomb stress term ($\Delta S(t)$ of equation (21)), the dilatancy/compaction effect term and the evolution effect term in
 407 equation (21). Figure 3 shows these three terms for $U = 1$ and $U = 0.01$. For $U = 1$, the amplitude of the dotted
 408 blue line representing the tidal Coulomb stress and the amplitude of the solid black line representing the
 409 dilatancy/compaction effect are almost the same, and there is a slight phase difference between them. Representing
 410 this phase difference as $\beta (\ll \pi)$, we see from the balance between the solid black line and the dot blue line in Figure
 411 3 that $-\mu_{pl} U \sigma_{eff}^0 \log(\theta/\theta_{pl}) \sim |\Delta S(t)| e^{i\omega(t-\beta)}$. The dashed black line representing the evolution effect is negligibly
 412 small ($b \sigma_{eff}^0 \log(\theta/\theta_{pl}) \sim 0$). Substituting these into equation (21), and after some algebra (Appendix B), we find
 413 that

$$414 \quad \log\left(\frac{V}{V_{pl}}\right) \propto \text{Re}\left\{e^{i\omega\left(t+\frac{\pi}{2}\right)}\right\}. \quad (22)$$

415 This formula indicates that the slip velocity peak agrees with the tidal Coulomb stress rate peak ($T_\theta/T \sim 10^1$ in the
 416 black line of Figure 2a). For $U = 0.01$, the phase difference δ is small ($T_\theta/T \sim 10^0$ in the blue line of Figure 2a).
 417 This difference can be explained by considering the balance in equation (21). The amplitude of the solid yellow line
 418 representing the dilatancy/compaction effect in equation (21) is smaller than the amplitude of the dotted blue line
 419 representing the tidal Coulomb stress. Furthermore, the dashed yellow line representing the evolution effect

420 decreases when the dilatancy/compaction effect term (solid yellow line) is larger and vice versa. Therefore, the
421 amplitude of the sum of these two effects becomes even smaller than the amplitude of $\Delta S(t)$. For the stress balance
422 of equation (21) to be satisfied, the direct effect term (second term on the RHS) should balance the difference
423 between $\Delta S(t)$ and the sum of the above two effects. This means that for a smaller U , a larger direct effect is
424 needed. The dominance of the direct effect term indicates that δ is small, as we have seen for the case of $T_\theta/T \gg$
425 $|b - \mu_{pl}U|/a$, which explains why δ is closer to zero for $U = 0.01$ than for $U = 1$, as shown by Figure 2 (Figure S5
426 shows the time variation of the tidal Coulomb stress term ($\Delta S(t)$ of equation (21)), the dilatancy/compaction effect
427 term and the evolution effect term in equation at $U = 0.1$).

428 Figure S6 schematically illustrates how the pore fluid (dilatancy/compaction effect), tidal stresses and
429 fault creep velocity generally evolve during one tidal oscillation. Because the case for $U = 1$ can
430 reproduce the observations at both stages of the ETS, we show only the case for $U = 1$.



431

432 Figure 2. (a) The numerical solution of α (dots) and the approximation solution (equation (19)) (solid line). From

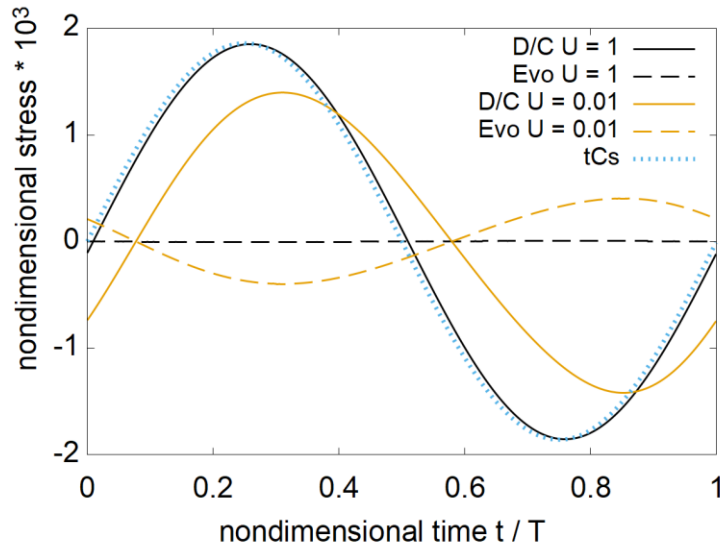
433 equation (19), we can derive $\alpha = 1/(a - b + \mu_0 U)\sigma_{eff}^0$ when $T_\theta/T \ll 1$ and $\alpha = 1/a\sigma_{eff}^0$ when $T_\theta/T \gg$

434 $|b - \mu_{pl}U|/a$. Specific values for $U = 0.01$ are displayed in the figure at $T_\theta/T \gg |b - \mu_{pl}U|/a$ and at $T_\theta/T \ll 1$.

435 (b) The numerical solution of δ (dots) and the approximation solution (equation (20)) (solid line). The differences in

436 color represent the differences in the dilatancy parameter U .

437



438

439 Figure 3. Time evolution of the tidal Coulomb stress (tCs) (blue dotted line), the dilatancy/compaction effect (D/C)
 440 (solid lines), and the evolution effect (Evo) (dashed lines) in equation (21). The horizontal axis denotes time
 441 normalized by the tidal cycle, and the values from 0 to 1 indicate one tidal cycle. The vertical axis denotes the tidal
 442 Coulomb stress/frictional strength normalized by σ_{eff}^0 . The numerical solutions for $T_\theta/T = 14$ and $U = 1$ are
 443 shown in black, and those for $T_\theta/T = 1.4$ and $U = 0.01$ are shown in yellow.

444

445 4 Discussion

446 4.1 Application of the model to the observed tidal response during the ETS

447 As mentioned in the introduction, most of the previous models are unable to account for the phase difference of
 448 $\delta \sim \pi/2$, which is observed at the early stage of ETS. As shown below, our model reproduces the tidal response
 449 during the ETS, including the phase difference, for a specific range of fault physical properties constrained by
 450 experiments, geological studies, and numerical modeling.

451 The observed tidal responses typically show $\alpha \lesssim 0.1 \text{ kPa}^{-1}$ and $\delta \sim \pi/2$ at the early stage of the ETS and
 452 $\alpha \sim 0.7 \text{ kPa}^{-1}$ and $\delta \sim 0$ at the later stage of the ETS. The slip velocity of the fault, which rapidly increases at the
 453 onset of the ETS, decreases to below steady-state subduction velocity with the progress of the ETS. In our model,
 454 ETS is represented by setting V_{pl} higher than the steady-state subduction velocity (Table 2). Considering that

455 $V_{pl} \sim 10^{-8} \sim 10^{-6}$ m/s, at the moment, we assume $V_{pl} \sim 10^{-6}$ m/s at the early stage of the ETS and $V_{pl} \sim 10^{-8}$ m/s at the
 456 later stage.

457 4.2.1 The ranges of U reproduce the observation

458 We see from Figure 2a and 2b that the model reproduces the observed tidal response at the early stage of ETS ($\alpha \lesssim$
 459 0.1 , $\delta \sim \pi/2$) when $T_\theta/T \sim 10$ and $U \sim 1$. This case corresponds to the last of the three categories of T_θ/T presented
 460 in section 3.2.3. We have seen that the first term on the RHS of equation (21) (the dilatancy/compaction effect term),
 461 which has a phase delay with respect to the tidal Coulomb stress change, dominates in the frictional strength change,
 462 and δ becomes $\pi/2$. The dominance of the dilatancy/compaction effect term reduces the direct effect term, which
 463 results in a smaller variation in the slip velocity ($\alpha \lesssim 0.1$). For $V_{pl} = 10^{-6}$ m/s, we obtain $d_c = 10^{-1}$ m from the
 464 condition of $T_\theta/T \sim 10$ (equation (15)).

465 Up to this point, we have used the undrained model. The drained model assumes that the pore fluid pressure
 466 diffuses outside the shear zone, as shown in equation (S1). This implies that the shear zone has a high permeability.
 467 From text S1 and S2 in the supporting information, we derived the dilatancy parameter (E_p) in the drained model
 468 and estimated the valid range of the parameter. Within the range, the drained model can reproduce α for both the
 469 initial and later stages by assuming $d_c = 10^{-2}$ m (the solid black line in Figure S3a in the supporting information).
 470 However, the drained model cannot reproduce $\delta \sim \pi/2$ at the early stage (Figure S3b in the supporting information).
 471 In addition, we confirmed that even when the dilatancy parameter is an order of magnitude larger than the
 472 reasonable value, we cannot reproduce $\delta \sim \pi/2$ at the early stage (Figure S7 in the supporting information). The
 473 result that only the undrained model can reproduce both α and δ suggests the low permeability of the shear zone.
 474 This indicates the possibility that our model can constrain the frictional parameters and the dilatancy coefficient as
 475 well as a hydraulic property of the fault through a comparison with observations of tidal response.

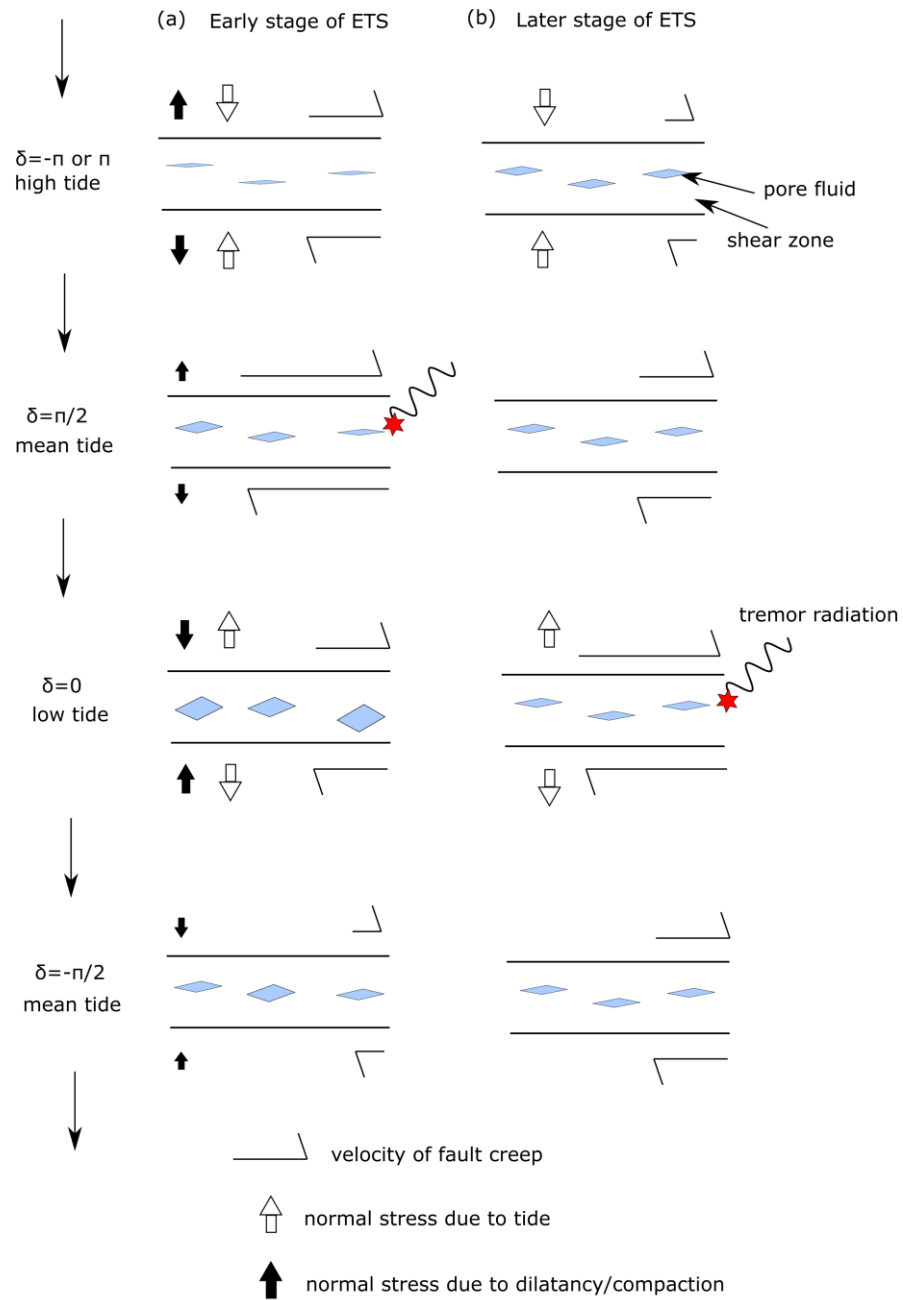
476 Here, we return to the application of the undrained model. Focusing on the case of $U \sim 1$, which explains the early
 477 stage, we see that the model can reproduce the observed tidal response at the later stage of the ETS ($\alpha \sim 0.7$ kPa $^{-1}$
 478 and $\delta \sim 0$) when $T_\theta/T \gtrsim 10^3$. This case corresponds to $T_\theta/T \gg |b - \mu_{pl}U|/a$ described in the three categories in
 479 section 3.2.3. As noted above, the phase advance disappears ($\delta \sim 0$) as the direct effect term (second term) on the
 480 RHS of equation (21) becomes dominant in the frictional strength change, and α asymptotically reaches a value that
 481 is independent of U ($\alpha \sim 1/a\sigma_{eff}^0$). For $V_{pl} = 10^{-8}$ m/s, the condition of $T_\theta/T \gtrsim 10^3$ indicates that $d_c \gtrsim 10^{-1}$ m.

482 On the other hand, Figure 2a shows that the model for $U = 0.01$ and $U = 0.1$ can explain the tidal response at the
483 later stage of ETS when $d_c \gtrsim 10^{-3}$ m and $d_c \gtrsim 10^{-2}$ m, respectively. This means that if we apply the model only
484 to the tidal response at the later stage of ETS, d_c might be underestimated.

485 The above comparison between the model and observations shows that the dilatancy/compaction effect is dominant
486 at the early stage of the ETS, while the dilatancy/compaction effect is negligible at the later stage of the ETS. Figure
487 4 schematically illustrates the physical process suggested by our model. First, we see the early stage of ETS (Figure
488 4a). A higher tide level increases the ocean load and reduces $\Delta S(t)$. At low tide ($\delta \sim 0$), $\Delta S(t)$ takes its maximum.
489 However, the effect generated by the low tide is almost canceled out by the significant increase in the normal stress
490 due to the dilatancy/compaction effect. At the mean tide ($\delta \sim \pi/2$), $\Delta S(t)$ is zero. The dilatancy/compaction effect is
491 reduced but still able to decrease the normal stress. Consequently, the slip velocity or the tremor rate reaches the
492 maximum. Next, we see the later stage of ETS (Figure 4b). Since the dilatancy/compaction effect is always
493 negligible at this stage, the slip velocity is maximized when $\Delta S(t)$ becomes the largest (low tide).

494 Incidentally, we can reproduce the observed tidal response (α, δ) as well as the observation that the number of
495 tremors decreases by one or two orders of magnitude at the later stage of ETS compared to that at the early stage.
496 This is because in equation (2), the tremor rate is proportional to the fault creep velocity, meaning that the tremor
497 rate at the later stage of the ETS ($V_{pl} \sim 10^{-8}$ m/s) is two orders of magnitude less than the tremor rate at the early
498 stage of the ETS ($V_{pl} \sim 10^{-6}$ m/s).

499



500

501 Figure 4. A schematic illustration of the relationship between the fault creep velocity and tide level. For simplicity,

502 only the normal stress change is represented. (a) Early stage of ETS. The sum of the normal stress due to the

503 dilatancy/compaction effect (black arrows) and the tidal normal stress (white arrows) becomes the largest in the

504 sense of enhancing fault slip at $\delta \sim \pi/2$. (b) Later stage of ETS. The dilatancy/compaction effect is negligible, and

505 the fault creep velocity reaches its maximum at $\delta \sim 0$.

506

507 4.2.2 The ranges of d_c reproduce the observation

508 In section 4.2.1, we showed that the observation can be reproduced when $d_c \sim 10^{-1}$ m, assuming $V_{pl} \sim 10^{-8 \sim -6}$ m/s.

509 On the other hand, Figure 5 (a) and (b) show that the observation cannot be reproduced when d_c is other than

510 $\sim 10^{-1}$ m. For example, when $d_c = 10^{-3}$, $\alpha \sim 0$ and $\delta \sim 0$ at the early stage of ETS ($V_{pl} \sim 10^{-6}$ m/s) and $\alpha \sim 0$

511 and $\delta \sim \pi/2$ at the later stage of ETS ($V_{pl} \sim 10^{-8}$ m/s).

512 The above range of $d_c \sim 10^{-1}$ m, which explains the observation, was determined from the conditions that

513 $T_\theta/T \sim 10$ at the early stage of ETS and $T_\theta/T \gg |b - \mu_{pl}U|/a$ (~ 100) at the later stage of ETS. In principle,

514 these two conditions can be met for any V_{pl} if d_c is appropriately chosen, considering the form of equation (15). In

515 practice, however, d_c can be constrained based on V_{pl} estimated from observations and numerical simulations.

516 Based on observations and simulations, the slip velocity of the SSE is $10^{-9 \sim -6}$ m/s (e.g., Goswami and Barbot

517 2018; Schwartz and Rokosky, 2007; Segall et al. 2010). The slip velocity of the fault, which rapidly increases at

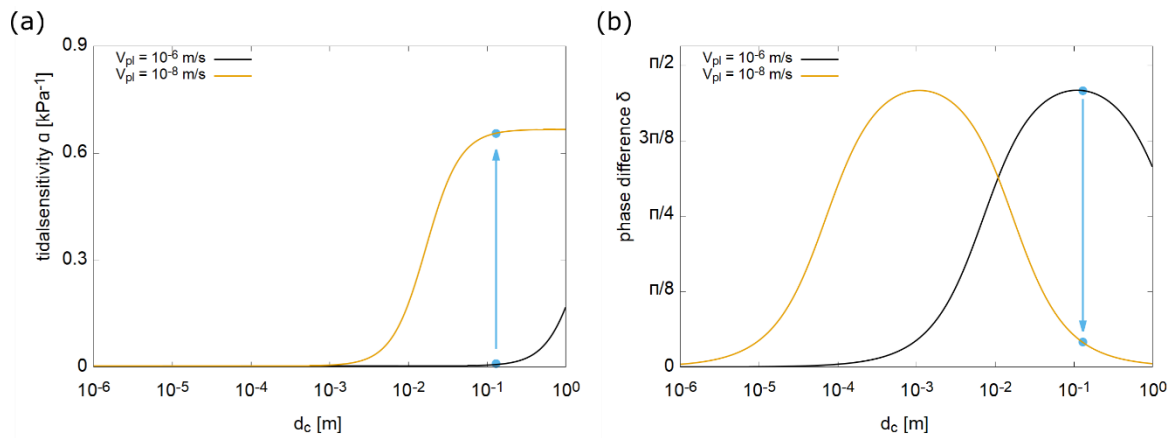
518 the onset of the ETS, decreases to the inter-ETS period velocity with the progress of the ETS. Based on the above

519 conditions, we can reproduce the observation not only for $V_{pl} \sim 10^{-8 \sim -6}$ m/s but also for $V_{pl} \sim 10^{-9 \sim -7}$ m/s by

520 employing $d_c = 10^{-2}$ (Figure S8). When d_c is other than 10^{-2} m, the observation cannot be reproduced.

521 Therefore, our model and observations are consistent for critical slip distances of 0.1-0.01 m in the transition

522 zone.



523
 524 Figure 5. (a) The approximation solution of α (equation (19)) when $V_{pl} = 10^{-6}$ m/s (black) and
 525 10^{-8} m/s (yellow). The horizontal axis denotes the critical slip distance d_c . The blue dots show that α
 526 for $d_c = 0.13$ m increases from $\lesssim 0.1$ to ~ 0.7 as V_{pl} decreases from 10^{-6} m/s to 10^{-8} m/s. (b) The

527 same as in (a) but for the approximation solution of δ (equation (20)). The blue dots show that δ
 528 decreases from $\sim\pi/2$ to ~ 0 as V_{pt} decreases from 10^{-6} m/s to 10^{-8} m/s.

529

530 4.3 The constrained physical fault properties

531 For our model to simultaneously reproduce the observed tidal responses at the early and later stages of the ETS, the
 532 following four conditions must be satisfied: $U(= M\epsilon/\sigma_{eff}^0)\sim 1$, $d_c\sim 10^{-1}$ m, the occurrence of
 533 dilatancy/compaction in the fault creep region (i.e., $a > b$) and low permeability within the shear zone (undrained
 534 model). Below, we discuss the validity of these conditions.

535 4.3.1 The dilatancy parameter U

536 Samuelson et al. (2009) obtained a dilatancy coefficient, and Segall et al. (1995) obtained bulk moduli of the fluid
 537 and pore space. These results yield $\epsilon\sim 10^{-4\sim-5}$ and $M\sim 10^{10}$ Pa (equation (7)). We assume that these experimentally
 538 obtained values are of the same magnitude in the transition zone. Substituting these values into $U(= \epsilon M/\sigma_{eff}^0) = 1$,
 539 which reproduces the observed tidal response, we obtain $\sigma_{eff}^0 = \epsilon M U \sim 10^{5\sim 6}$ Pa, which supports a near-lithostatic
 540 pore fluid pressure (e.g., Audet et al., 2009; Nakata, 2008; Shelly et al., 2006; Yabe et al., 2015).

541 4.3.2 The critical slip distance d_c

542 The results of friction experiments on rocks and gouges show $d_c\sim 10^{-4\sim-6}$ m (e.g., Marone, 1998). Our results
 543 ($d_c\sim 10^{-1\sim 2}$ m) are 2~5 orders of magnitude larger. The much larger critical slip distance can be explained by
 544 considering the differences in roughness between laboratory surfaces and natural faults (Scholz et al., 1988) and the
 545 differences in the thickness of the shear zone between experimental and natural faults (Marone and Kilgore, 1993).

546 Numerical models assuming the RSF also adopt a critical slip distance larger than that in the experimental results.
 547 For example, Nakata et al. (2012) successfully modeled the SSE and aftershocks after the $\sim M7$ earthquake in
 548 Hyuga-nada, Japan, with $d_c = 10^{-1\sim 0}$ m. Maury et al. (2014) calculated a time evolution of shear stress for the SSE
 549 in Mexico and estimated that the critical slip distance that can quantitatively reproduce the observed results is
 550 5×10^{-2} m. Kawamura et al. (2018) applied a 1-D multidegree of freedom spring-slider model with $d_c = 10^{-2}$ m

551 to reproduce various types of fault slip, such as fast slip, source nucleation, aftershock, and SSE. Our analysis of the
 552 tidal response during ETS also supports d_c with the order of $10^{-1\sim-2}$ m.

553 4.3.3 The occurrence of dilatancy/compaction in the fault creep region

554 Numerical models that have been proposed thus far generally require the presence of a VW region ($a - b < 0$) to
 555 reproduce SSE (e.g., Liu and Rice, 2005; Segall et al., 2010). Some models have proposed a mechanism by which
 556 SSE occurs in the VS regime, such as the generation of a negative Coulomb stress change due to fault valve action
 557 (Perfettini and Ampuro 2008) and the transition of the RSF from the VW at low speeds to the VS at high speeds
 558 (e.g., Im et al., 2020; Peng and Rubin, 2018; Shibazaki and Iio, 2003). Our model employs the framework of the VS
 559 and expresses the velocity of the slow slip by V_{pl} phenomenologically.

560 The above two models assuming the VS (e.g., Im et al., 2020; Peng and Rubin, 2018; Perfettini and Ampuro, 2008;
 561 Shibazaki and Iio 2003) do not consider the time variation of pore fluid pressure. On the other hand, Beeler et al.
 562 (2018) developed a model that considers the time variation of pore fluid pressure in the VW region. However, it
 563 cannot be applicable to the tidal modulation of the tremor rate during ETS. Our results show that when we assume
 564 the framework of the VS, the observed tidal response at the early stage of ETS cannot be reproduced unless
 565 dilatancy/compaction occurs.

566 4.3.4 The fluid pressure diffusivity derived from the undrained condition

567 For the undrained model, $T \ll t_w$ must be satisfied (section 2.2.2). Using this condition, we can quantitatively
 568 constrain the fluid pressure diffusivity as follows. We assume that the thickness of the shear zone is w and the fluid
 569 pressure diffusivity in the shear zone is c_{hyd}^* . Then, a dimensional analysis shows that $w \sim \sqrt{t_w c_{hyd}^*}$, where t_w
 570 denotes the characteristic timescale on which the pore fluid pressure diffuses through the shear zone. Therefore, the
 571 condition of $T \ll t_w$ can be rewritten as $T \ll w^2 / c_{hyd}^*$.

572 We estimate w in the transition zone in the following manner since it cannot be observed directly. A drilling
 573 investigation and structural analyses of drill cores on the Nojima Fault revealed that w in the seismogenic zone is
 574 $\sim 10^{1/2}$ m (Lin and Nishikawa, 2019). It is generally expected that w in the VS region is larger than in the VW
 575 region (e.g., Chen and Rampel, 2015). Therefore, we assume $w \sim 10^{0\sim 1/2}$ m in the VS region. Then, the above
 576 undrained condition yields $c_{hyd}^* \ll 2 * 10^{-5\sim-4}$ m²/s. This value of c_{hyd}^* is consistent with Branut (2021), who

577 reported that the observed rupture propagation of an SSE could be reproduced by a crack propagation model at
 578 $w \sim 6 \text{ cm}$ and $c_{hyd}^* \sim 10^{-6} \text{ m}^2/\text{s}$. Previous studies have shown that the c_{hyd}^* of the seismogenic zone is
 579 $\sim 10^{-8 \sim -3} \text{ m}^2/\text{s}$ (Yamashita and Tsutsumi, 2018). Our results suggest that the shear zone in the transition zone is
 580 probably as impermeable as that in the seismogenic zone.

581 4.4 Other effects than dilatancy/compaction

582 We have seen that the dilatancy/compaction effect is important to explain the phase difference ($\delta \sim \pi/2$) in the tidal
 583 response. In this section, we examine whether other effects could explain $\delta \sim \pi/2$. The following two possibilities
 584 are considered.

585 In the first case, a change in the state variable is introduced due to the normal stress acting on the fault plane
 586 (Linker and Dieterich, 1992). In this case, the time variation of the state variable can be written as follows:

$$587 \quad \frac{d\theta}{dt} = -\frac{V\theta}{d_c} \log\left(\frac{V\theta}{d_c}\right) - \frac{\gamma \dot{\sigma}}{b\sigma} \theta, \quad (23)$$

588 where γ is a constitutive parameter representing a normal stress dependence. In general, $\gamma \sim O(0.1)$. Therefore, we
 589 adopt $\gamma = 0.2$ and solve the governing equations of our model replacing the evolution law (equation (4)) with
 590 equation (23). The results indicate that the difference caused by considering the effect of normal stress on the state
 591 variable is less than 1%. Therefore, the influence of the Linker-Dieterich effect is small and does not provide a
 592 reason for the large phase difference.

593 In the second case, tidal Coulomb stress can directly destroy the tremor source instead of aseismic slip on the
 594 surrounding fault. This effect is ignored in our model. If this is the case, the tremor rate is proportional to the tidal
 595 Coulomb stressing rate (i.e., $\delta \sim \pi/2$) (Beeler et al., 2013; Lockner and Beeler, 1999). This direct effect of the tidal
 596 Coulomb stress should become clearer when the aseismic slip on the surrounding fault is smaller, i.e., at the later
 597 stage of the ETS (Royer et al., 2015). However, the observed result shows $\delta \sim 0$ at the later stage, indicating that the
 598 direct effect is smaller.

599 None of the above effects can explain the phase difference of $\delta \sim \pi/2$, and thus, the pore fluid pressure change due
 600 to dilatancy/compaction is more likely to cause the large phase difference at the early stage of the ETS.

601 4.5 Application to the tidal response of continuous families

602 By setting the value of V_{pl} to a steady-state plate convergence velocity (e.g., 10^{-9} m/s), we can examine the range
 603 of d_c and U in which our model reproduces the tidal response of continuous families. The observations show that
 604 the tidal response of continuous families is $\delta \sim 0$ (Ide and Tanaka, 2014; Thomas et al., 2012) and $\alpha \sim 1.5 \text{ kPa}^{-1}$
 605 (Thomas et al., 2012), for example. We examine whether these observations can be reproduced with parameters that
 606 reproduce the tidal response of episodic families ($d_c \sim 10^{-1}$ m, $U \sim 1$) (section 4.2). In the case of $d_c = 10^{-1}$ m,
 607 $V_{pl} = 10^{-9}$ m/s and $T_\theta/T \sim 10^4$, we obtain $\alpha \sim \alpha \sigma_{eff}^0 (= 0.67 \text{ kPa}^{-1})$ and $\delta \sim 0$ (section 3.2.2). Therefore, by slightly
 608 reducing the value of σ_{eff}^0 , the tidal responses of continuous families and episodic families can be reproduced with
 609 similar values of the fault physical properties.

610 4.6 Limitations of our model

611 Our model, in which fault creep is represented with a one-degree-of-freedom spring block of the VS regime ($a -$
 612 $b > 0$), necessarily fails to include the occurrence of slow slip accompanying a rapid release of the accumulated
 613 stress. For this reason, we expressed the occurrence of slow slip by the difference in V_{pl} and assumed that the tremor
 614 rate during ETS is proportional to the fault creep velocity (equation (2)). Our model accounted for the tidal response
 615 of tremors during ETS, but this does not hold if the frictional law requires $a - b < 0$ during SSE. In such a case, our
 616 model needs to be extended to include unstable regions ($a - b < 0$) by increasing the degrees of freedom.

617 Models that assume $a - b < 0$, which have been proposed thus far, include models with complex fault geometries
 618 (Romanet et al., 2018), 3-D elastic media (Matsuzawa et al., 2010), heterogeneous fault physical properties (Luo and
 619 Ampuero, 2018), and nonuniform permeability in space and time (Bizzarri, 2012; Cappa, 2011; Dunham and Rice,
 620 2008). They account for more complex effects that are not considered in our model. However, the tidal response of
 621 these models has not yet been investigated.

622 Because our model adopts a one-degree-of-freedom (one-DOF) spring-slider system, it cannot simulate the
 623 spatiotemporal variation in stress during an ETS. Such spatiotemporal changes in stress have been modeled using a
 624 two-dimensional system (e.g., Hawthorne and Rubin, 2013), which can reproduce observations such as a spatial
 625 propagation of ETS and temporal changes in the slip velocity during ETS. Hawthorne and Rubin (2013) examined
 626 the tidal response of ETS based on such a 2-D model.

627 However, Hawthorne and Rubin (2013) reported that the tidal response during ETS obtained by a 2-D simulation
 628 qualitatively agrees with the tidal response of the one-DOF ramp block slider model. Their model does not include
 629 the effect of dilatancy/compaction. To confirm whether the one-DOF and 2-D simulation results are in agreement
 630 for a model including the dilatancy/compaction effect, we need to extend our model to a 2-D system. One approach
 631 to do so would be to incorporate the dilatancy/compaction effect considered in our model into the model of
 632 Hawthorne and Rubin (2013).

633 **5 Conclusions**

634 Tremors in the transition zone are sensitive to tidal stress. In this study, we propose a physical model to explain the
 635 tidal response of tremors observed during the ETS. Following previous studies (Ader et al., 2012; Beeler et al.,
 636 2013; Shelly et al., 2007a), we assumed that tremors are generated by the rupture of a small brittle patch on the fault
 637 plane due to the aseismic shear slip of a larger-scale surrounding fault. As in Ader et al. (2012), we adopted a one-
 638 degree-of-freedom spring-slider that follows the RSF for the VS and set up the governing equations to describe the
 639 slip behavior of the block, considering a pore fluid pressure change in the shear zone (section 2). We considered
 640 drained (high-permeability) and undrained (low-permeability) models and presented results are mainly of the
 641 undrained model, which could reproduce more observations than the drained model. The inclusion of pore pressure
 642 changes due to dilatancy/compaction in the VS regime is in remarkable contrast to previous theoretical models
 643 describing tidal modulation.

644 In our model, the tidal response is expressed with the tidal sensitivity (α), which represents the amplitude of the
 645 tidal modulation of fault creep velocity, and the phase difference (δ) of the fault creep velocity peak relative to the
 646 tidal Coulomb stress peak. We analytically derived an approximate solution to reveal how the tidal response depends
 647 on the fault physical properties in section 3. We note that the slip behavior is primarily controlled by the
 648 characteristic timescale $T_\theta (= 2\pi d_c/V_{pl})$ at which the state variable evolves, where d_c is the critical slip distance
 649 and V_{pl} is the background fault creep. We found that the behavior of α and δ can be classified into three cases
 650 according to the magnitude of T_θ/T ($T_\theta/T \gg |b - \mu_{pl}U|/a$, $T_\theta/T \sim |b - \mu_{pl}U|/a$, $T_\theta/T \ll 1$), where T is the
 651 tidal cycle (~ 12 hours), a and b are frictional constitutive parameters, μ_{pl} is the frictional coefficient and U is the
 652 dilatancy parameter. This classification reflects the degree to which the dilatancy/compaction effect is dominant in

653 the frictional strength change. We showed that the smaller T_θ/T is, the more dominant the dilatancy/compaction
 654 effect is in the friction strength change.

655 We applied the model to ETS, assuming that V_{pl} changes between the early and later stages of the ETS. The model
 656 successfully reproduced the tidal response observed at both stages of the ETS. Adopting this undrained model, we
 657 constrained the effective normal stress to be $10^{5\sim6}$ Pa, the critical slip distance to be $10^{-1\sim-2}$ m, and the fluid
 658 pressure diffusivity to be 10^{-5} m²/s or less. Of particular importance is the use of the phase difference in the
 659 estimation of the fault properties. Without considering the dilatancy/compaction effect, the phase difference at the
 660 early stage cannot be reproduced. Moreover, using the tidal response data obtained during only the early stage or the
 661 later stage produces different estimates of the fault properties. The range of the fault properties obtained in our study
 662 are in the ranges inferred by independent studies. Our model supports a critical slip distance of $\sim 10^{-1\sim-2}$ m, which
 663 has been used in numerical simulations of earthquake cycles. This study shows that the physical modeling of the
 664 tidal response of tremors during the ETS is an effective method to retrieve the fault properties in the transition zone,
 665 including hydraulic properties.

666

667 **Appendices**

668 **Appendix A: Derivation of equation (21)**

669 Substituting equation (3) into equation (8) and transforming the result, we obtain

$$\begin{aligned}
 670 \quad k\Delta u + \Delta\tau &= \left\{ \mu_0 + a \log\left(\frac{V_{pl}}{V_0}\right) + b \log\left(\frac{\theta_{pl}}{\theta_0}\right) + a \log\left(\frac{V}{V_{pl}}\right) + b \log\left(\frac{\theta}{\theta_{pl}}\right) \right\} \sigma_{eff} \\
 671 \quad &= \left\{ \mu_{pl} + a \log\left(\frac{V}{V_{pl}}\right) + b \log\left(\frac{\theta}{\theta_{pl}}\right) \right\} \sigma_{eff}. \quad (A)
 \end{aligned}$$

672 We represent the relative displacement of the block at the steady state without the tide as Δu_{no} . Then, $k\Delta u_{no} =$
 673 $\mu_{pl}\sigma_{eff}^0$ holds, where the RHS is obtained by setting $\Delta\sigma(t) = 0$ and $\Delta p(t) = 0$ in equation (9). We can confirm that
 674 $k\Delta u \sim \mu_{pl}\sigma_{eff}^0$ as follows. For the parameter set in Table 2, $k\Delta\dot{u} \sim O(kV_{pl})$ is three orders of magnitude smaller than
 675 $\Delta\dot{\tau} \sim O(2\pi|\Delta\tau|/T)$. This means that $k\Delta\dot{u}$ on the LHS of the time derivative of equation (A) is negligibly small,
 676 suggesting that $\Delta u \sim \Delta u_{no}$. Replacing $k\Delta u$ with $\mu_{pl}\sigma_{eff}^0$ on the LHS and using equations (9) and (11), equation (A)
 677 can be rewritten as

678
$$\Delta S(t) = -\mu_{pl}\Delta p(t) + a\sigma_{eff}\log\left(\frac{V}{V_{pl}}\right) + b\sigma_{eff}\log\left(\frac{\theta}{\theta_{pl}}\right). \quad (B)$$

679 In equation (B), the LHS corresponds to the tidal Coulomb stress and the RHS corresponds to the frictional strength.

680 Furthermore, equation (B) can be written as

681
$$\Delta S(t) \sim -\mu_{pl}U\sigma_{eff}^0\log\left(\frac{\theta}{\theta_{pl}}\right) + a\sigma_{eff}^0\log\left(\frac{V}{V_{pl}}\right) + b\sigma_{eff}^0\log\left(\frac{\theta}{\theta_{pl}}\right) \quad (C)$$

682 by using equation (7), where $\Delta p = 0$ is taken at $\theta = \theta_{pl}$, and it is assumed that the changes in the effective normal

683 stress in the second and third terms on the RHS of equation (C) are sufficiently small compared to σ_{eff}^0 .

684 **Appendix B: Derivation of equation (22)**

685 Substituting $-\mu_{pl}U\sigma_{eff}^0\log(\theta/\theta_{pl}) \sim \Delta S e^{i\omega(t-\beta)}$ and $b\sigma_{eff}^0\log(\theta/\theta_{pl}) \sim 0$ into equation (21), as described in section

686 3.2.3, we obtain

687
$$\log\left(\frac{V}{V_{pl}}\right) \sim |\Delta S(t)| \operatorname{Re}(e^{i\omega t} - e^{i\omega(t-\beta)}). \quad (D)$$

688 When $\theta_1 = \omega t - \beta/2$, $\theta_2 = \beta/2$, we can write $\operatorname{Re}(e^{i\omega t} - e^{i\omega(t-\beta)}) = \cos(\theta_1 + \theta_2) - \cos(\theta_1 - \theta_2) =$

689 $\sin(\theta_1) \sin(\theta_2)$. Using $\sin(\theta_1) = \cos(\pi/2 + \theta_1)$, we obtain $\sin(\theta_1) \sin(\theta_2) = \cos(\omega t + (\pi - \beta)/2) \sin(\beta/2)$.

690 That is, $\log(V/V_{pl}) \sim |\Delta S(t)| \sin(\beta/2) \cos(\omega t + (\pi - \beta)/2)$. Furthermore, since $\beta \ll \pi$, equation (D) can be

691 rewritten as

692
$$\log\left(\frac{V}{V_{pl}}\right) \sim |\Delta S(t)| \sin\left(\frac{\beta}{2}\right) \operatorname{Re}\left\{e^{i(\omega t + \frac{\pi}{2})}\right\}. \quad (E)$$

693 **Open Research**

694 The source code is available from zenodo ([10.5281/zenodo.6403829](https://zenodo.org/doi/10.5281/zenodo.6403829)).

695 **Acknowledgments**

696 We thank Dr. Takehito Suzuki for the valuable discussion of an earlier version of this work. We acknowledge

697 Associate Editor, Kate Huishuan Chen, and the anonymous reviewer for their comments that helped us improve the

698 article. For this study, we used the computer systems of the Earthquake and Volcano Information Center of the

699 Earthquake Research Institute, The University of Tokyo. This work was supported by JSPS KAKENHI Grant

700 Numbers JP16H02219, JP16H06474, JP21H01187 and JP21H05204.

701 **References**

- 702 Ader, T. J., Ampuero, J. P., & Avouac, J. P. (2012). The role of velocity-neutral creep on the modulation of tectonic
703 tremor activity by periodic loading. *Geophysical research letters*, 39(16). <https://doi.org/10.1029/2012GL052326>
- 704 Audet, P., Bostock, M. G., Christensen, N. I., & Peacock, S. M. (2009). Seismic evidence for overpressured
705 subducted oceanic crust and megathrust fault sealing. *Nature*, 457(7225), 76-78.
706 <https://doi.org/10.1038/nature07650>
- 707 Audet, P., & Bürgmann, R. (2014). Possible control of subduction zone slow-earthquake periodicity by silica
708 enrichment. *Nature*, 510(7505), 389-392. <https://doi.org/10.1038/nature13391>
- 709 Bartlow, N. M., Lockner, D. A., & Beeler, N. M. (2012). Laboratory triggering of stick - slip events by oscillatory
710 loading in the presence of pore fluid with implications for physics of tectonic tremor. *Journal of Geophysical*
711 *Research: Solid Earth*, 117(B11). <https://doi.org/10.1029/2012JB009452>
- 712 Bartlow, N. M., Miyazaki, S. I., Bradley, A. M., & Segall, P. (2011). Space-time correlation of slip and tremor
713 during the 2009 Cascadia slow slip event. *Geophysical Research Letters*, 38(18).
714 <https://doi.org/10.1029/2011GL048714>
- 715 Beeler, N. M., & Lockner, D. A. (2003). Why earthquakes correlate weakly with the solid Earth tides: Effects of
716 periodic stress on the rate and probability of earthquake occurrence. *Journal of Geophysical Research: Solid*
717 *Earth*, 108(B8). <https://doi.org/10.1029/2001JB001518>
- 718 Beeler, N. M., Thomas, A., Bürgmann, R., & Shelly, D. (2013). Inferring fault rheology from low-frequency
719 earthquakes on the San Andreas. *Journal of Geophysical Research: Solid Earth*, 118(11), 5976-5990.
720 <https://doi.org/10.1002/2013JB010118>
- 721 Beeler, N. M., Thomas, A., Bürgmann, R., & Shelly, D. (2018). Constraints on friction, dilatancy, diffusivity, and
722 effective stress from low-frequency earthquake rates on the deep San Andreas Fault. *Journal of Geophysical*
723 *Research: Solid Earth*, 123(1), 583-605. <https://doi.org/10.1002/2017JB015052>
- 724 Bizzarri, A. (2012). Effects of permeability and porosity evolution on simulated earthquakes. *Journal of structural*
725 *geology*, 38, 243-253. <https://doi.org/10.1016/j.jsg.2011.07.009>
- 726 Brantut, N. (2021). Dilatancy toughening of shear cracks and implications for slow rupture propagation. *Journal of*
727 *Geophysical Research: Solid Earth*, 126(11), e2021JB022239. <https://doi.org/10.1029/2021JB022239>

- 728 Cappa, F. (2011). Influence of hydromechanical heterogeneities of fault zones on earthquake ruptures. *Geophysical*
729 *Journal International*, 185(2), 1049-1058. <https://doi.org/10.1111/j.1365-246X.2011.04994.x>
- 730 Chanard, K., Nicolas, A., Hatano, T., Petrelis, F., Latour, S., Vinciguerra, S., & Schubnel, A. (2019). Sensitivity of
731 acoustic emission triggering to small pore pressure cycling perturbations during brittle creep. *Geophysical Research*
732 *Letters*, 46(13), 7414-7423. <https://doi.org/10.1029/2019GL082093>
- 733 Chen, J., & Rempel, A. W. (2015). Shear zone broadening controlled by thermal pressurization and poroelastic
734 effects during model earthquakes. *Journal of Geophysical Research: Solid Earth*, 120(7), 5215-5237.
735 <https://doi.org/10.1002/2014JB011641>
- 736 Chen, K. H., Tai, H. J., Ide, S., Byrne, T. B., & Johnson, C. W. (2018). Tidal modulation and tectonic implications
737 of tremors in Taiwan. *Journal of Geophysical Research: Solid Earth*, 123(7), 5945-5964.
738 <https://doi.org/10.1029/2018JB015663>
- 739 Cochran, E. S., Vidale, J. E., & Tanaka, S. (2004). Earth tides can trigger shallow thrust fault
740 earthquakes. *Science*, 306(5699), 1164-1166. [10.1126/science.1103961](https://doi.org/10.1126/science.1103961)
- 741 Dieterich, J. H. (1979). Modeling of rock friction: 1. Experimental results and constitutive equations. *Journal of*
742 *Geophysical Research: Solid Earth*, 84(B5), 2161-2168. <https://doi.org/10.1029/JB084iB05p02161>
- 743 Dragert, H., Wang, K., & James, T. S. (2001). A silent slip event on the deeper Cascadia subduction
744 interface. *Science*, 292(5521), 1525-1528. <https://doi.org/10.1126/science.1060152>
- 745 Dunham, E. M., & Rice, J. R. (2008). Earthquake slip between dissimilar poroelastic materials. *Journal of*
746 *Geophysical Research: Solid Earth*, 113(B9). <https://doi.org/10.1029/2007JB005405>
- 747 Goswami, A., & Barbot, S. (2018). Slow-slip events in semi-brittle serpentinite fault zones. *Scientific reports*, 8(1),
748 1-11. <https://doi.org/10.1038/s41598-018-24637-z>
- 749 Hawthorne, J. C., & Rubin, A. M. (2013). Tidal modulation and back-propagating fronts in slow slip events
750 simulated with a velocity-weakening to velocity-strengthening friction law. *Journal of Geophysical Research: Solid*
751 *Earth*, 118(3), 1216-1239. <https://doi.org/10.1002/jgrb.50107>
- 752 Heaton, T. H. (1982). Tidal triggering of earthquakes. *Bulletin of the Seismological Society of America*, 72(6A),
753 2181-2200. <https://doi.org/10.1785/BSSA07206A2181>

- 754 Hirose, H., Hirahara, K., Kimata, F., Fujii, N., & Miyazaki, S. I. (1999). A slow thrust slip event following the two
755 1996 Hyuganada earthquakes beneath the Bungo Channel, southwest Japan. *Geophysical Research Letters*, *26*(21),
756 3237-3240. <https://doi.org/10.1029/1999GL010999>
- 757 Hirose, H., & Obara, K. (2010). Recurrence behavior of short-term slow slip and correlated nonvolcanic tremor
758 episodes in western Shikoku, southwest Japan. *Journal of Geophysical Research: Solid Earth*, *115*(B6).
759 <https://doi.org/10.1029/2008JB006050>
- 760 Houston, H. (2015). Low friction and fault weakening revealed by rising sensitivity of tremor to tidal stress. *Nature*
761 *Geoscience*, *8*(5), 409-415. <https://doi.org/10.1038/ngeo2419>
- 762 Ide, S. (2010). Striations, duration, migration and tidal response in deep tremor. *Nature*, *466*(7304), 356-359.
763 <https://doi.org/10.1038/nature09251>
- 764 Ide, S., Shelly, D. R., & Beroza, G. C. (2007). Mechanism of deep low frequency earthquakes: Further evidence that
765 deep non-volcanic tremor is generated by shear slip on the plate interface. *Geophysical Research Letters*, *34*(3).
766 <https://doi.org/10.1029/2006GL028890>
- 767 Ide, S., & Tanaka, Y. (2014). Controls on plate motion by oscillating tidal stress: Evidence from deep tremors in
768 western Japan. *Geophysical Research Letters*, *41*(11), 3842-3850. <https://doi.org/10.1002/2014GL060035>
- 769 Ide, S., Yabe, S., Tai, H. J., & Chen, K. H. (2015). Thrust-type focal mechanisms of tectonic tremors in Taiwan:
770 Evidence of subduction. *Geophysical Research Letters*, *42*(9), 3248-3256. <https://doi.org/10.1002/2015GL063794>
- 771 Im, K., Saffer, D., Marone, C., & Avouac, J. P. (2020). Slip-rate-dependent friction as a universal mechanism for
772 slow slip events. *Nature Geoscience*, *13*(10), 705-710. <https://doi.org/10.1038/s41561-020-0627-9>
- 773 Ito, Y., Obara, K., Shiomi, K., Sekine, S., & Hirose, H. (2007). Slow earthquakes coincident with episodic tremors
774 and slow slip events. *Science*, *315*(5811), 503-506. <https://doi.org/10.1126/science.1134454>
- 775 Kawamura, H., Yamamoto, M., & Ueda, Y. (2018). Slow-Slip Phenomena Represented by the One-Dimensional
776 Burridge–Knopoff Model of Earthquakes. *Journal of the Physical Society of Japan*, *87*(5), 053001.
777 <https://doi.org/10.7566/JPSJ.87.053001>
- 778 Lin, A., & Nishiwaki, T. (2019). Repeated seismic slipping events recorded in a fault gouge zone: Evidence from
779 the Nojima fault drill holes, SW Japan. *Geophysical Research Letters*, *46*(3), 1276-1283.
780 <https://doi.org/10.1029/2019GL081927>

- 781 Linker, M. F., & Dieterich, J. H. (1992). Effects of variable normal stress on rock friction: Observations and
782 constitutive equations. *Journal of Geophysical Research: Solid Earth*, 97(B4), 4923-4940.
783 <https://doi.org/10.1029/92JB00017>
- 784 Liu, Y. (2013). Numerical simulations on megathrust rupture stabilized under strong dilatancy strengthening in slow
785 slip region. *Geophysical Research Letters*, 40(7), 1311-1316. <https://doi.org/10.1002/grl.50298>
- 786 Liu, Y., & Rice, J. R. (2005). Aseismic slip transients emerge spontaneously in three-dimensional rate and state
787 modeling of subduction earthquake sequences. *Journal of Geophysical Research: Solid Earth*, 110(B8).
788 <https://doi.org/10.1029/2004JB003424>
- 789 Lockner, D. A., & Beeler, N. M. (1999). Premonitory slip and tidal triggering of earthquakes. *Journal of*
790 *Geophysical Research: Solid Earth*, 104(B9), 20133-20151. <https://doi.org/10.1029/1999JB900205>
- 791 Luo, Y., & Ampuero, J. P. (2018). Stability of faults with heterogeneous friction properties and effective normal
792 stress. *Tectonophysics*, 733, 257-272. <https://doi.org/10.1016/j.tecto.2017.11.006>
- 793 Luo, Y., & Liu, Z. (2019). Rate-and-state model casts new insight into episodic tremor and slow-slip variability in
794 Cascadia. *Geophysical Research Letters*, 46(12), 6352-6362. <https://doi.org/10.1029/2019GL082694>
- 795 Matsuzawa, T., Hirose, H., Shibasaki, B., & Obara, K. (2010). Modeling short-and long-term slow slip events in the
796 seismic cycles of large subduction earthquakes. *Journal of Geophysical Research: Solid Earth*, 115(B12).
797 <https://doi.org/10.1029/2010JB007566>
- 798 Marone, C. (1998). Laboratory-derived friction laws and their application to seismic faulting. *Annual Review of*
799 *Earth and Planetary Sciences*, 26(1), 643-696. <https://doi.org/10.1146/annurev.earth.26.1.643>
- 800 Marone, C., & Kilgore, B. (1993). Scaling of the critical slip distance for seismic faulting with shear strain in fault
801 zones. *Nature*, 362(6421), 618-621. <https://doi.org/10.1038/362618a0>
- 802 Marone, C., Raleigh, C. B., & Scholz, C. H. (1990). Frictional behavior and constitutive modeling of simulated fault
803 gouge. *Journal of Geophysical Research: Solid Earth*, 95(B5), 7007-7025.
804 <https://doi.org/10.1029/JB095iB05p07007>
- 805 Maury, J., Aochi, H., & Radiguet, M. (2014). Fault constitutive relations inferred from the 2009-2010 slow slip
806 event in Guerrero, Mexico. *Geophysical Research Letters*, 41(14), 4929-4936.
807 <https://doi.org/10.1002/2014GL060691>

- 808 Meade, B. J., & Loveless, J. P. (2009). Predicting the geodetic signature of $M_w \geq 8$ slow slip events. *Geophysical*
809 *Research Letters*, 36(1). <https://doi.org/10.1029/2008GL036364>
- 810 Métivier, L., de Viron, O., Conrad, C. P., Renault, S., Diament, M., & Patau, G. (2009). Evidence of earthquake
811 triggering by the solid earth tides. *Earth and Planetary Science Letters*, 278(3-4), 370-375.
812 <https://doi.org/10.1016/j.epsl.2008.12.024>
- 813 Nakata, R., Hyodo, M., & Hori, T. (2012). Numerical simulation of afterslips and slow slip events that occurred in
814 the same area in Hyuga-nada of southwest Japan. *Geophysical Journal International*, 190(2), 1213-1220.
815 <https://doi.org/10.1111/j.1365-246X.2012.05552.x>
- 816 Nakata, R., Suda, N., & Tsuruoka, H. (2008). Nonvolcanic tremor resulting from the combined effect of Earth tides
817 and slow slip events. *Nature Geoscience*, 1(10), 676-678. <https://doi.org/10.1038/ngeo288>
- 818 Noël, C., Passelègue, F. X., Giorgetti, C., & Violay, M. (2019). Fault reactivation during fluid pressure oscillations:
819 Transition from stable to unstable slip. *Journal of Geophysical Research: Solid Earth*, 124(11), 10940-10953.
820 <https://doi.org/10.1029/2019JB018517>
- 821 Noël, C., Pimienta, L., & Violay, M. (2019). Time - dependent deformations of sandstone during pore fluid pressure
822 oscillations: Implications for natural and induced seismicity. *Journal of Geophysical Research: Solid Earth*, 124(1),
823 801-821. <https://doi.org/10.1029/2018JB016546>
- 824 Obara, K. (2002). Nonvolcanic deep tremor associated with subduction in southwest Japan. *Science*, 296(5573),
825 1679-1681. <https://doi.org/10.1126/science.1070378>
- 826 Obara, K., Hirose, H., Yamamizu, F., & Kasahara, K. (2004). Episodic slow slip events accompanied by non-
827 volcanic tremors in southwest Japan subduction zone. *Geophysical Research Letters*, 31(23).
828 <https://doi.org/10.1029/2004GL020848>
- 829 Peng, Y., & Rubin, A. M. (2018). Simulating Short-Term Evolution of Slow Slip Influenced by Fault
830 Heterogeneities and Tides. *Geophysical Research Letters*, 45(19), 10-269. <https://doi.org/10.1029/2018GL078752>
- 831 Perfettini, H., & Ampuero, J. P. (2008). Dynamics of a velocity strengthening fault region: Implications for slow
832 earthquakes and postseismic slip. *Journal of Geophysical Research: Solid Earth*, 113(B9).
833 <https://doi.org/10.1029/2007JB005398>
- 834 Perfettini, H., & Schmittbuhl, J. (2001). Periodic loading on a creeping fault: Implications for tides. *Geophysical*
835 *Research Letters*, 28(3), 435-438. <https://doi.org/10.1029/2000GL011686>

- 836 Proctor, B., Lockner, D. A., Kilgore, B. D., Mitchell, T. M., & Beeler, N. M. (2020). Direct evidence for fluid
837 pressure, dilatancy, and compaction affecting slip in isolated faults. *Geophysical Research Letters*, *47*(16).
838 <https://doi.org/10.1029/2019GL086767>
- 839 Rice, J. R. (2006). Heating and weakening of faults during earthquake slip. *Journal of Geophysical Research: Solid*
840 *Earth*, *111*(B5). <https://doi.org/10.1029/2005JB004006>
- 841 Rogers, G., & Dragert, H. (2003). Episodic tremor and slip on the Cascadia subduction zone: The chatter of silent
842 slip. *Science*, *300*(5627), 1942-1943. <https://doi.org/10.1126/science.1084783>
- 843 Romanet, P., Bhat, H. S., Jolivet, R., & Madariaga, R. (2018). Fast and slow slip events emerge due to fault
844 geometrical complexity. *Geophysical Research Letters*, *45*(10), 4809-4819. <https://doi.org/10.1029/2018GL077579>
- 845 Royer, A. A., Thomas, A. M., & Bostock, M. G. (2015). Tidal modulation and triggering of low-frequency
846 earthquakes in northern Cascadia. *Journal of Geophysical Research: Solid Earth*, *120*(1), 384-405.
847 <https://doi.org/10.1002/2014JB011430>
- 848 Rubinstein, J. L., La Rocca, M., Vidale, J. E., Creager, K. C., & Wech, A. G. (2008). Tidal modulation of
849 nonvolcanic tremor. *Science*, *319*(5860), 186-189. <https://doi.org/10.1126/science.1150558>
- 850 Ruina, A. (1983). Slip instability and state variable friction laws. *Journal of Geophysical Research: Solid*
851 *Earth*, *88*(B12), 10359-10370. <https://doi.org/10.1029/JB088iB12p10359>
- 852 Samuelson, J., Elsworth, D., & Marone, C. (2009). Shear-induced dilatancy of fluid-saturated faults: Experiment and
853 theory. *Journal of Geophysical Research: Solid Earth*, *114*(B12). <https://doi.org/10.1029/2008JB006273>
- 854 Savage, H. M., & Marone, C. (2007). Effects of shear velocity oscillations on stick - slip behavior in laboratory
855 experiments. *Journal of Geophysical Research: Solid Earth*, *112*(B2). <https://doi.org/10.1029/2005JB004238>
- 856 Scholz, C. H. (1988). The critical slip distance for seismic faulting. *Nature*, *336*(6201), 761-763.
857 <https://doi.org/10.1038/336761a0>
- 858 Scholz, C. H. (1998). Earthquakes and friction laws. *Nature*, *391*(6662), 37-42. <https://doi.org/10.1038/34097>
- 859 Scholz, C. H. (2019). *The mechanics of earthquakes and faulting*. New York, NY; Cambridge University Press.
860 <https://doi.org/10.1017/9781316681473>
- 861 Scholz, C. H., Tan, Y. J., & Albino, F. (2019). The mechanism of tidal triggering of earthquakes at mid-ocean
862 ridges. *Nature communications*, *10*(1), 1-7. <https://doi.org/10.1038/s41467-019-10605-2>

- 863 Schwartz, S. Y., & Rokosky, J. M. (2007). Slow slip events and seismic tremor at circum-Pacific subduction
864 zones. *Reviews of Geophysics*, 45(3). <https://doi.org/10.1029/2006RG000208>
- 865 Segall, P. (2010). *Earthquake and volcano deformation*. Princeton NJ: Princeton University Press.
866 <https://doi.org/10.1515/9781400833856>
- 867 Segall, P., & Rice, J. R. (1995). Dilatancy, compaction, and slip instability of a fluid-infiltrated fault. *Journal of*
868 *Geophysical Research: Solid Earth*, 100(B11), 22155-22171. <https://doi.org/10.1029/95JB02403>
- 869 Segall, P., Rubin, A. M., Bradley, A. M., & Rice, J. R. (2010). Dilatant strengthening as a mechanism for slow slip
870 events. *Journal of Geophysical Research: Solid Earth*, 115(B12). <https://doi.org/10.1029/2010JB007449>
- 871 Shelly, D. R., Beroza, G. C., & Ide, S. (2007a). Non-volcanic tremor and low-frequency earthquake
872 swarms. *Nature*, 446(7133), 305-307. <https://doi.org/10.1038/nature05666>
- 873 Shelly, D. R., Beroza, G. C., & Ide, S. (2007b). Complex evolution of transient slip derived from precise tremor
874 locations in western Shikoku, Japan. *Geochemistry, Geophysics, Geosystems*, 8(10).
875 <https://doi.org/10.1029/2007GC001640>
- 876 Shelly, D. R., Beroza, G. C., Ide, S., & Nakamura, S. (2006). Low-frequency earthquakes in Shikoku, Japan, and
877 their relationship to episodic tremor and slip. *Nature*, 442(7099), 188-191. <https://doi.org/10.1038/nature04931>
- 878 Shelly, D. R., Peng, Z., Hill, D. P., & Aiken, C. (2011). Triggered creep as a possible mechanism for delayed
879 dynamic triggering of tremor and earthquakes. *Nature Geoscience*, 4(6), 384-388. <https://doi.org/10.1038/ngeo1141>
- 880 Shibazaki, B., & Iio, Y. (2003). On the physical mechanism of silent slip events along the deeper part of the
881 seismogenic zone. *Geophysical Research Letters*, 30(9). <https://doi.org/10.1029/2003GL017047>
- 882 Shibazaki, B., Obara, K., Matsuzawa, T., & Hirose, H. (2012). Modeling of slow slip events along the deep
883 subduction zone in the Kii Peninsula and Tokai regions, southwest Japan. *Journal of Geophysical Research: Solid*
884 *Earth*, 117(B6). <https://doi.org/10.1029/2011JB009083>
- 885 Suzuki, T., & Yamashita, T. (2009). Dynamic modeling of slow earthquakes based on thermoporoelastic effects and
886 inelastic generation of pores. *Journal of Geophysical Research: Solid Earth*, 114(B6).
887 <https://doi.org/10.1029/2008JB006042>
- 888 Tan, Y. J., & Marsan, D. (2020). Connecting a broad spectrum of transient slip on the San Andreas fault. *Science*
889 *advances*, 6(33), eabb2489. <https://doi.org/10.1126/sciadv.abb2489>

- 890 Tanaka, S. (2012). Tidal triggering of earthquakes prior to the 2011 Tohoku - Oki earthquake (Mw
891 9.1). *Geophysical research letters*, 39(7). <https://doi.org/10.1029/2012GL051179>
- 892 Tanaka, S. (2010). Tidal triggering of earthquakes precursory to the recent Sumatra megathrust earthquakes of 26
893 December 2004 (Mw 9.0), 28 March 2005 (Mw 8.6), and 12 September 2007 (Mw 8.5). *Geophysical Research*
894 *Letters*, 37(2). <https://doi.org/10.1029/2009GL041581>
- 895 Thomas, A. M., Beeler, N. M., Bletery, Q., Burgmann, R., & Shelly, D. R. (2018). Using low-frequency earthquake
896 families on the San Andreas Fault as deep creepmeters. *Journal of Geophysical Research: Solid Earth*, 123(1), 457-
897 475. <https://doi.org/10.1002/2017JB014404>
- 898 Thomas, A. M., Bürgmann, R., Shelly, D. R., Beeler, N. M., & Rudolph, M. L. (2012). Tidal triggering of low
899 frequency earthquakes near Parkfield, California: Implications for fault mechanics within the brittle-ductile
900 transition. *Journal of Geophysical Research: Solid Earth*, 117(B5). <https://doi.org/10.1029/2011JB009036>
- 901 Thomas, A. M., Nadeau, R. M., & Bürgmann, R. (2009). Tremor-tide correlations and natthostatic pore pressure on
902 the deep San Andreas fault. *Nature*, 462(7276), 1048-1051. <https://doi.org/10.1038/nature08654>
- 903 van der Elst, N. J., Delorey, A. A., Shelly, D. R., & Johnson, P. A. (2016). Fortnightly modulation of San Andreas
904 tremor and low-frequency earthquakes. *Proceedings of the National Academy of Sciences*, 113(31), 8601-8605.
905 <https://doi.org/10.1073/pnas.1524316113>
- 906 Vidale, J. E., Agnew, D. C., Johnston, M. J., & Oppenheimer, D. H. (1998). Absence of earthquake correlation with
907 Earth tides: An indication of high preseismic fault stress rate. *Journal of Geophysical Research: Solid*
908 *Earth*, 103(B10), 24567-24572. <https://doi.org/10.1029/98JB00594>
- 909 Villafuerte, C., & Cruz-Atienza, V. M. (2017). Insights into the causal relationship between slow slip and tectonic
910 tremor in Guerrero, Mexico. *Journal of Geophysical Research: Solid Earth*, 122(8), 6642-6656.
911 <https://doi.org/10.1002/2017JB014037>
- 912 Wein, A. S., & Shearer, P. M. (2004, December). A comprehensive search for tidal triggering of Southern California
913 earthquakes. In *AGU Fall Meeting Abstracts* (Vol. 2004, pp. S23A-0297).
- 914 Yabe, S., Tanaka, Y., Houston, H., & Ide, S. (2015). Tidal sensitivity of tectonic tremors in Nankai and Cascadia
915 subduction zones. *Journal of Geophysical Research: Solid Earth*, 120(11), 7587-7605.
916 <https://doi.org/10.1002/2015JB012250>

- 917 Yamashita, T., & Tsutsumi, A. (2018). *Involvement of fluids in earthquake ruptures*. Tokyo, Japan: Springer.
- 918 <https://doi.org/10.1007/978-4-431-56562-8>